Journal of Colloid and Interface Science **215,** 140–158 (1999)
Article ID jcis.1999.6253, available online at http://www.idealibrary.com on IDEAL®

Sorption of Metal Ions on Clay Minerals

I. Polarized EXAFS Evidence for the Adsorption of Co on the Edges of Hectorite Particles

Michel L. Schlegel,*[,1] Alain Manceau,* Daniel Chateigner,† and Laurent Charlet*

*Environmental Geochemistry Group, LGIT-IRIGM, University of Grenoble, BP 53, F-38 041 Grenoble Cedex 9, France; and †Laboratoire de Physique de l'État Condensé, Université du Maine, BP535, F-72085 Le Mans Cedex 9, France

E-mail: Michel.Schlegel@ujf-grenoble.fr

Received November 25, 1998; accepted March 30, 1999

The local structural environment of Co sorbed on hectorite (a magnesian smectite) has been investigated by polarized EXAFS (P-EXAFS) spectroscopy on a self-supporting film of Co-sorbed hectorite. This sorption sample was prepared by contacting Co and hectorite at pH 6.5 and at high ionic strength (0.3 M $NaNO_3$) to favor pH-dependent sorption reaction over cation exchange. A self-supporting film was elaborated after 120 h of reacting time, when apparent quasi-equilibrium conditions were attained. The half-width at half maximum of the orientation distribution of c* axis of individual clay platelets off the film normal was determined by quantitative texture analysis, and found to be equal to 18.9°. Co K-edge P-EXAFS spectra were recorded at angles between the incident beam and the film normal equal to 0°, 35°, 50°, and 60°; the 90° spectrum was obtained by extrapolation. Spectral analysis led to the identification of the two nearest cationic subshells containing 1.6 ± 0.4 Mg at 3.03 Å and 2.2 ± 0.5 Si at 3.27 Å. These distances are respectively characteristic of edge-sharing linkages between Mg and Co octahedra and of corner-sharing linkages between Co octahedra and Si tetrahedra, as in clay structures. The angular dependence of the Co–Mg and Co–Si contributions indicates that Co–Mg pairs are oriented parallel to the film plane, whereas Co–Si pairs are not. These results are interpreted by the formation of Co inner-sphere mononuclear surface complexes located at the edges of hectorite platelets, in the continuity of the (Mg, Li) octahedral sheet.

Key Words: **Co; hectorite; adsorption; EXAFS; polarized EXAFS; surface complex.**

INTRODUCTION

Smectites are widespread minerals of weathering formations and sediments (1). They possess a large specific surface area and a high structural charge (up to 1000 meq per kg). Therefore, these clay minerals much influence the physico-chemical properties of geological formations where they are present. The retention properties of smectites are also of interest for the setup of geochemical barriers for nuclear waste repositories. These barrier systems are foreseen to limit leaching of hazardous chemicals or radionuclides (2). Industrial applications of smectites encompass heterogeneous catalysis on modified clays (3) and pharmacological technologies. For all these reasons, a good understanding of the surface stability and sorptive reactivity of smectites is highly desirable.

The high surface reactivity of smectites is a direct consequence of their lamellar and defective structure. Smectites are built of layers made by the condensation of one central octahedral sheet and two tetrahedral sheets (4). Heteroionic cationic substitutions impart to smectites a permanent negative structural charge, which is compensated by the adsorption of cations on basal planes. Divalent cations sorbed on these planes form outer-sphere (OS) surface complexes (5–10) and are easily exchanged with solute ions by varying the cationic composition of the solution. Besides these cation exchange properties, smectites also possess pH-dependent sorption properties (11–17). The pH-dependent sorption was inferred to take place at layer edges, where truncation of the bulk structure leads to the formation of oxygen dangling bonds. However, no definite structural evidence for the adsorption of cations on edge sites has been reported yet. Extended X-ray absorption fine structure (EXAFS) studies rather suggested that the pH-dependent sorption of cations on phyllosilicates leads to the precipitation of mixed (18, 19) or pure (9, 20) hydroxide phases, without definite evidence for spatial association between the precipitated and the sorbent phases. Furthermore, a recent reevaluation of EXAFS data on a similar sorbate–sorbent system (21) emphasized the relatively high uncertainty on structural parameters (interatomic distance, number of neighboring atoms) obtained by powder-EXAFS, which could eventually bring the reliability of several sorption structural models in question. One origin for these uncertainties is the relatively limited reciprocal space explored by EXAFS (at best $\Delta k = 14$ $Å^{-1}$), which prevents the discrimination of atomic shells separated by less than 0.10–0.15 Å (22). This is typically the case in phyllosilicates, where absorbing atoms of the octahedral sheet are surrounded by neighboring cations from the octahe-

[1] To whom correspondence should be addressed.

0021-9797/99 $30.00

dral and tetrahedral sheets at $R \sim 3.05$–3.10 Å and $R \sim 3.20$–3.25 Å, respectively. Manceau and co-workers (23, 24) showed that this limitation can be overcome by performing polarized-EXAFS (P-EXAFS) experiments on phyllosilicate single crystals. The contribution of cations from the tetrahedral sheets can be minimized by orienting the phyllosilicate plane parallel to the electric field vector ϵ of the incident X-ray beam (Fig. 1, left). Conversely, the contribution of cations from the octahedral sheet is extinguished in the perpendicular orientation of ϵ (Fig. 1, right). Recently, this P-EXAFS technique was successfully applied for the first time to well-textured self-supporting clay films (25, 26). These studies demonstrated the unique ability of P-EXAFS to probe highly anisotropic environments with an enhanced precision, as compared to powder EXAFS. The discriminating capacity of P-EXAFS can be used to differentiate cations precipitated in solution from cations adsorbed on the edges of smectite layers.

In the present study, the sorption mechanism of Co on hectorite, a magnesian smectite, was investigated by P-EXAFS spectroscopy performed on a self-supporting film of Co-sorbed hectorite. Adsorption of Co on the edge sites of hectorite was favored by carefully controlling the chemical conditions of the sorption process. In particular, sorption was carried out at high ionic strength ($I = 0.3$ M) to inhibit Co adsorption on cation exchange sites, and at moderate pH (pH 6.5) and Co concentration ([Co] $= 10^{-4}$ M) to avoid as much as possible the precipitation of either pure $Co(OH)_{2(s)}$ or of Co hydrous phyllosilicates such as Co-rich kerolite (hereafter referred to as CoKer) (21). The orientation distribution of hectorite crystallites in the self-supporting film plane was determined by quantitative texture analysis (QTA). Mg and Si cationic shells surrounding sorbed Co were unambiguously identified by P-EXAFS spectroscopy, and the orientation of the Co–Mg and Co–Si pairs with respect to the basal plane of hectorite particles were determined. Based on these results, a structural model for the adsorption mechanism of Co on the layer edges of hectorite is proposed.

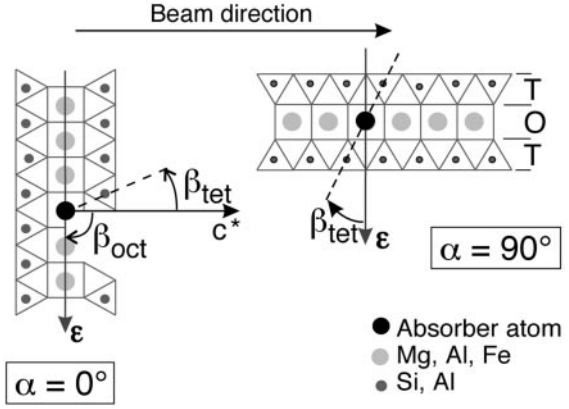

FIG. 1. Principle of polarized EXAFS measurements on phyllosilicates: (left) electric field vector ϵ parallel to the layer plane; (right) ϵ perpendicular to the layer plane.

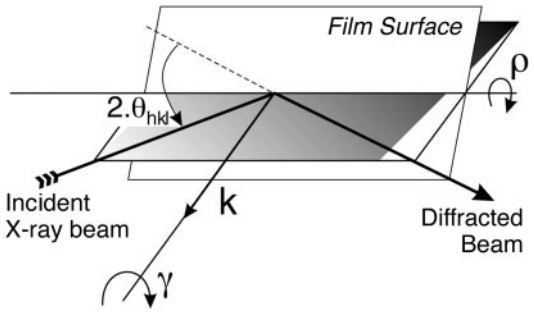

FIG. 2. X ray diffraction geometry used for texture analysis in the reflection mode. A θ_{hkl} pole figure can be measured by fixing θ_{hkl} and then rotating the sample around γ and ρ (both rotations conserving θ_{hkl}).

BACKGROUND

Quantitative Texture Analysis

The quantitative texture analysis of a polycrystalline aggregate is based on the concept of orientation distribution (OD), which represents a statistical description of the individual crystallite orientations within this aggregate (27). This orientation can be evaluated by determining the pole distribution of $\{hkl\}$ diffracting planes (i.e. the orientation distribution of the vectors $\langle hkl \rangle^*$ perpendicular to these planes) with respect to the sample referential. Figure 2 illustrates the principle of a pole distribution measurement on an X-ray diffractometer. Three rotation movements, θ_{hkl} (Bragg angle), γ (azimuthal angle), and ρ (tilt angle) are available. In this geometry, only $\{hkl\}$ planes whose poles are aligned with the **k** direction are in diffracting conditions, provided θ_{hkl} fulfills the Bragg condition. The diffracted intensity $I_{hkl}(\gamma, \rho)$ is proportional to the number of crystallite planes that satisfy these orientation and Bragg conditions. Rotation of the sample in every position around γ and ρ conserves θ_{hkl} and allows for all crystallites of the sample to be brought successively in a diffracting position. A pole density $P_{hkl}(\gamma, \rho)$ is then obtained by normalizing measured diffracted intensities with respect to an average value obtained by integrating all intensities over γ and ρ This normalization procedure enables the comparison of several samples regardless of their porosity and purity, under the assumption that the average diffracted intensity is constant whatever the true texture is. Finally, a pole figure is obtained by projecting the pole density on the film plane using an equal-area projection for qualitative visual representation of the textural quality of the sample.

In the case of smectite samples, only a few $\{hkl\}$ reflections are experimentally accessible, because some are too low θ_{hkl} angles to ensure a constant irradiation of the sample, and others are systematically extinct. Furthermore, the measurable peaks consist of several overlapped reflections, as a result of the

crystal symmetry (26), and the resulting multipole figures are of complex visual interpretation. To derive a quantitative information on the sample texture, it is then necessary to calculate the complete OD that would best fit the measured pole density, using a refinement technique. The quality of the fit between the experimental and the OD-recalculated pole density can be evaluated by the reliability factor,

$$RP = \frac{1}{I} \sum_{hkl} \sum_{j} \frac{P_{hkl}^{\text{calc}}(j) - P_{hkl}^{\text{obs}}(j)}{P_{hkl}^{\text{obs}}(j)}, \quad [1]$$

where $P_{hkl}^{\text{obs}}(j)$ and $P_{hkl}^{\text{calc}}(j)$ refer to the observed and recalculated pole densities, and j runs for all γ and ρ values. A similar reliability factor R_{w}, in which observed and recalculated intensities are weighed, can be defined. R_{w} enables the comparison of the refinement quality for samples with different texture strengths. Once the OD has been refined, every desired single pole figure can be recalculated for much simpler interpretation. More details on QTA refinements can be found elsewhere (26, 28).

Polarized EXAFS

In an EXAFS experiment, the absorption coefficient μ of an element present in the studied material is measured as a function of the energy of the incident X-ray beam. For a linearly polarized X-ray beam and a layered compound having a threefold or higher symmetry axis perpendicular to the layer plane, this absorption coefficient can be written (23–26, 29)

$$\mu^{\alpha} = \mu^{\parallel}\cos^2\alpha + \mu^{\perp}\sin^2\alpha, \quad [2]$$

where α is the angle between the electric field vector $\boldsymbol{\epsilon}$ and the layer plane (Fig. 1). The notations $\parallel$ and $\perp$ denote orientations of $\boldsymbol{\epsilon}$ parallel ($\alpha = 0°$) and perpendicular ($\alpha = 90°$) to the layer plane, respectively. The net EXAFS oscillations are derived from X-ray absorption spectra by the normalization equation

$$\chi = \frac{\mu - \mu_0}{\mu_0} \Rightarrow \mu = \mu_0(1 - \chi), \quad [3]$$

where μ_0 is the absorption coefficient of an isolated atom. As μ_0 does not depend on α, χ exhibits a dichroic angular dependence described by

$$\chi^{\alpha} = \chi^{\parallel}\cos^2\alpha + \chi^{\perp}\sin^2\alpha = \chi^{\perp} + (\chi^{\parallel} - \chi^{\perp})\cos^2\alpha. \quad [4]$$

Equation [4] is rigorously correct for the total macroscopic EXAFS signal (i.e. for the sum of single and multiple scattering contributions). From the knowledge of $\chi^{\parallel}$ and $\chi^{\perp}$, Eq. [4] allows the calculation of χ^{α} for any value of α in dichroic systems. Conversely, if $\chi^{\perp}$ is not accessible experimentally, then it can be calculated via linear regression of EXAFS spectra obtained for $\alpha < 90°$ and extrapolation to $\alpha = 90°$. In a perfectly disordered (isotropic) powder, χ^{α} is averaged over all space directions and reduces to an α-independent spectrum, χ^{iso}.

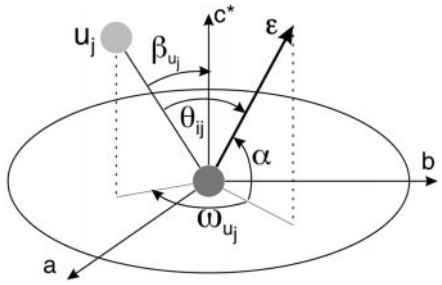

FIG. 3. Definition of the angles θ_{ij}, ω_{uj}, α, and β_{uj} in polarized experiments.

The EXAFS oscillations are interpreted microscopically as resulting from the interference between photoelectronic waves outgoing from the absorbing atom (i) and waves backscattered by neighboring atoms (j); therefore it can be decomposed into contributions of successive atomic shells, χ_{ij}. For a powder, the amplitude of χ_{ij}^{iso} is of course proportional to the number of atoms present in the j shell; N_j^{real} and χ_{ij}^{iso} can be written

$$\chi_{ij}^{\text{iso}} = S_0^2 N_j^{\text{real}} A_{ij}(k, \lambda, R_{ij}, \sigma_j) \cdot \sin(2kR_{ij} + \phi_{ij}(k)), \quad [5]$$

where k is the norm of the photoelectron wavevector, R_{ij} is the absorber–backscatterer distance, $\phi_{ij}(k)$ is a phase shift function depending on the nature of the ij pair, S_0^2 is an amplitude reduction factor which is characteristic of the absorber, and $A_{ij}(k, \lambda, R_{ij}, \sigma_j)$ is a damping function which depends on R_{ij}, on the mean free path of the photoelectron (λ), and on the structural and thermal disorder of the j shell, expressed as a Debye–Waller factor σ_j. At a given temperature, the more disordered the shell, the higher σ_j.

In contrast to powder EXAFS, in P-EXAFS the amplitude of χ_{ij}^{P} is not only dependent on N_j^{real}, but also on the orientation of $\boldsymbol{\epsilon}$ with respect to the vectors $\mathbf{R}_{iu_j}$ that connects the absorbing i atom to the u_j^{th} atom of the j shell. At the K-edge and in the plane-wave approximation, this relationship can be written

$$\chi_{ij}^{\text{P}} = 3\chi_{ij}^{\text{iso}} \sum_{u_j=1}^{N_j^{\text{real}}} \cos^2\theta_{iu_j} = 3\langle\cos^2\theta_{iu_j}\rangle\chi_{ij}^{\text{iso}}, \quad [6]$$

where θ_{iu_j} is the angle between $\boldsymbol{\epsilon}$ and $\mathbf{R}_{iu_j}$. The summation is made over all the N_j^{real} atoms of the j shell. For layered compounds, θ_{iu_j} can be expressed as a function of α, of the β_{u_j} angle between $\mathbf{R}_{iu_j}$ and $\mathbf{c}^*$, and of the ω_{u_j} angle between the in-plane projections of $\boldsymbol{\epsilon}$ and $\mathbf{R}_{iu_j}$ (Fig. 3). The existence of a threefold or higher symmetry axis normal to the layer plane indicates that the j^{th} shell contains several u_j backscattering atoms with the same β_{u_j} orientation (except for $\beta_{u_j} = 0°$).

Thus, the $\langle \cos^2\theta_{iu_j}\rangle$ term can be reduced to a function of only α and β_j by averaging the in-plane ω_{u_j} angles (29). This results in

$$3\langle \cos^2\theta_{iu_j}\rangle = 1 - \frac{(3\cos^2\beta_j - 1)(3\cos^2\alpha - 2)}{2}. \quad [7]$$

Hence the angular dependence of χ_{ij}^{P} can be described by a simple affine function of $\cos^2\alpha$:

$$\chi_{ij}^{P} = \chi_{ij}^{iso}\cdot\left[1 - \frac{(3\cos^2\beta_j - 1)(3\cos^2\alpha - 2)}{2}\right]. \quad [8]$$

Equation [8] confirms that only the amplitude of χ_{ij}^{P} is modified by varying α. It is then possible to define for each α angle an apparent number of neighboring backscatterers, N_j^{app}, which is proportional to χ_{ij}^{P}, so that

$$\frac{N_j^{app}}{N_j^{real}} = \frac{\chi_{ij}^{P}}{\chi_{ij}^{iso}}. \quad [9]$$

N_j^{app} can be calculated from β_j and N_j^{real} for any α value by combining Eqs. [8] and [9]:

$$N_j^{app} = N_j^{real}\cdot\left[1 - \frac{(3\cos^2\beta_j - 1)(3\cos^2\alpha - 2)}{2}\right]. \quad [10]$$

Equation [10] resumes to a simple expression in two cases. First, when $\alpha = 35.3°$, then $N_j^{app} = N_j^{real}$ regardless of β_j, and the polarized and powder EXAFS spectra are identical. Second, when $\beta_j = 53.7°$, $N_j^{app} = N_j^{real}$ regardless of α, and the EXAFS contribution of the j shell has no angular dependence. $\alpha = 35.3°$ and $\beta_j = 54.7°$ are "magic angles." Equation [10] also indicates that N_j^{app} increases with increasing α for $\beta_j < 54.7°$ and decreases with increasing α for $\beta_j > 54.7°$. Thus, the orientation of the ij pairs with respect to $\beta = 54.7°$ can be determined from the angular dependence of N_j^{app}.

How these theoretical considerations apply to phyllosilicates will now be shown taking Fe in biotite as a example (23, 24). Biotite is a trioctahedral phyllosilicate like hectorite (Fig. 1). Fe is located in the octahedral sheet and is surrounded by 6 (Fe, Mg) neighbors of the octahedral sheet ($\beta = 90°$) and 4 (Si, Al) neighbors of the tetrahedral sheets ($\beta \approx 33°$). These two shells are located at close distances (~3.04–3.10 Å vs 3.25–3.30 Å), and their EXAFS contributions cannot be discriminated by conventional EXAFS analysis (22), thereby decreasing the accuracy of the spectral quantitative analysis (30). In contrast, Eq. [10] shows that in P-EXAFS, the contribution from the (Fe, Mg) shell extinguishes for $\alpha = 90°$ ($N_{Fe,Mg}^{app} = 0$), and the analysis of the enhanced contribution of the single (Si, Al) shell is facilitated ($N_{Si,Al}^{app} = 8.4$). Likewise, for $\alpha = 0°$, the apparent number of (Si, Al) neighbors is diminished ($N_{Si,Al}^{app} = 1.8$), which makes easier the analysis of the enhanced contribution of the (Fe, Mg) shell ($N_{Fe,Mg}^{app} = 9$). Manceau and co-workers (23) confirmed experimentally these theoretical predictions and demonstrated that P-EXAFS measurements allow the determination of structural parameters (R_{ij}, N_j) for close atomic shells with an enhanced precision.

For an absorbing element whose structural environment is not known, the inclination angle β_j of a backscattering j shell with respect to **c*** can be ideally determined from the angular dependence of N_j^{app}. For this purpose, Eq. [10] can be rewritten as an affine function of $\cos^2\alpha$:

$$\frac{N_j^{app}}{N_j^{real}} = \frac{3}{2}(1 - 3\cos^2\beta_j)\cdot\cos^2\alpha + 3\cos^2\beta_j. \quad [11]$$

The slope (B) of this function depends only on β_j, and the β_j value can be readily determined from a linear regression of N_j^{app}/N_j^{real} with respect to $\cos^2\alpha$.

Eqs. [2], [4], [7]–[11] hold true for dichroic single crystals. They can be applied to textured self-supporting clay films, provided a symmetry axis of order greater than two exists normal to the film plane. For example, a C_∞ axis can be obtained by perfectly orienting the basal planes of individual platelets parallel to the film surface, and then dispersing the **a** and **b** axis randomly in the film plane. In this case, all **c*** axes point perpendicular to the film plane, and β_j are the same for all crystallites. For real films, in which the basal planes of platelets are disoriented off the film plane, a C_∞ axis can still be defined, if **a** and **b** axes are distributed randomly around the film normal. In this case, however, disorientation of the platelets causes a dispersion of the β_j angles and results in angular dependencies of N_j^{app} that are weaker than in the case of a perfect orientation. As a corollary, β_j determined experimentally from Eq. [11] on these real films tends to be underestimated for $\beta_j > 54.7°$ and overestimated for $\beta_j < 54.7°$.

EXPERIMENTAL

Hectorite Purification and Characterization

Hectorite $Na_{0.40}(Mg_{2.65}Li_{0.35})(Si_{3.95}Al_{0.05})O_{10}(OH)_2$ was purchased from the Clay Mineral Repository (SHCa-1). In this magnesian smectite, the Mg and Li atoms are located in the octahedral sheet and Si atoms in the tetrahedral sheets. Approximately 25 g of the raw material were suspended in 1 L of deionized Milli-Q water and shaken at 180 rpm for 48 h. The <2 μm fraction was then separated by sedimentation techniques. This fraction was treated several times with a 10^{-4} mol L^{-1} (M) HNO_3 solution to remove carbonate minerals, and subsequently washed 5 times with 0.5 M NaCl to exchange interlayer cations with sodium. No concentrated inorganic acid solutions were used, since hectorite appears to dissolve quickly in strong acidic media (31, 32). Afterwards the clay suspension was treated 1 h with a 5×10^{-3} M dithionite, 0.2 M citrate, 0.1

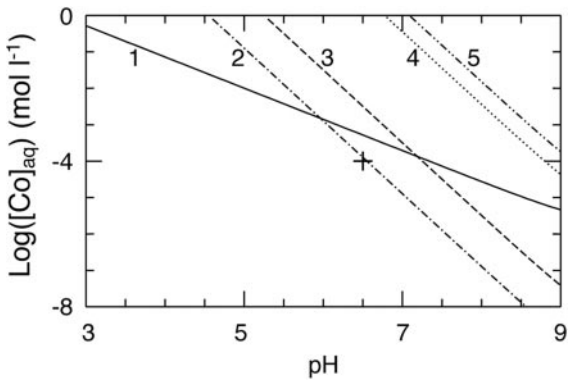

FIG. 4. Solubility of Co in solution with respect to Co hydroxides and Co-rich kerolite (CoKer). Solubility constants are taken from Refs. (21, 74). Plots of solubility limits are given for (1) stoichiometric dissolution of CoKer, (2) CoKer solubility controlled by amorphous silica, (3) CoKer solubility controlled by quartz, (4) solubility of pink active Co hydroxide, and (5) solubility of blue Co hydroxide. The cross refers to the maximal experimental [Co] in the hectorite suspension.

M bicarbonate, 0.5 M NaCl solution at pH 6.5 to remove possibly remaining ferric oxides, and 1 h with a 3% H_2O_2, 0.5 M NaCl solution at 50°C to remove organic matter (17, 33, 34). Remaining H_2O_2 was destroyed by heating the suspension for more than 1 h at 70°C. Dialysis against Milli-Q water was then performed until no Cl^- anions could be detected ($AgNO_3$ test). The final 2 wt% stock suspension was stored at 4°C in the dark prior to use. Measurements of aqueous SiO_2 concentrations at different preparation stages showed that the amorphous-SiO_2 solubility limit was never reached.

The purified clay suspension was characterized by X-ray diffraction on a Siemens D-500 X-ray diffractometer. No trace of crystallized carbonate mineral could be detected. The cation exchange capacity (CEC), measured by Cs exchange (35), is 840 meq kg^{-1}. Specific surface area determined by BET equals 114 m^2 g^{-1}.

Co sorption and Film Preparation

General Considerations

Chemical reactions such as hectorite dissolution, formation of pure or mixed Co hydroxide, or Co adsorption on exchange sites may strongly interfere with Co adsorption on pH-dependent sites. Therefore, the chemical conditions (pH, ionic strength) for Co sorption were carefully determined to avoid these interferences.

The lower limit of the possible pH value for Co sorption was imposed by the dissolution kinetics of hectorite. At pH 6.5, it takes about 10 days for the working clay suspension to reach a free Si concentration of 400 μM. Since the dissolution rate of hectorite is enhanced at lower pH (36), pH 6.0 was chosen as a lower limit. Also, as a prerequisite, pH has to be high enough to allow for a sufficient amount of Co to sorb on hectorite within a reasonable period of time. The upper pH limit was selected to avoid precipitation of pure $Co(OH)_{2(s)}$ and CoKer. Plots of the Co solubility with respect to CoKer and $Co(OH)_{2(s)}$ (Fig. 4) indicate that the upper pH limit for Co sorption is ~6.7 for a Co concentration of 100 μM. Sorption experiments were thus conducted at pH 6.5.

Ionic strength (I) and equilibration time for Co sorption were defined on the basis of kinetic results obtained at two different ionic strengths (Fig. 5). At low ionic strength (0.01 M $NaNO_3$), an important Co sorption occurred within the first 5 min of contact time between the cation and the clay surface. At high ionic strength (0.3 M $NaNO_3$), this rapid cation sorption was far less pronounced, which suggests that it corresponds to Co adsorption on exchange sites (37). Following this initial step, sorption went on at slower rates. The relaxation time associated with this second sorption step is not compatible with a cation exchange process (37). Based on these results, Co was sorbed at high ionic strength (I = 0.3 M) to inhibit cation exchange, and the self-supporting film was elaborated after 120 h of reacting time, when Co sorption was significantly slowed down.

Experimental Design

All chemicals were of ACS reagent grade. All solutions were prepared with Milli-Q water. A constant Na concentration of 0.3 M was maintained throughout the experiment by preparing the working solutions with the appropriate amounts of $NaNO_3$ salt (Fluka). pH measurements were made using a Metrohm combined electrode connected to a Metrohm pH-meter. This electrode was calibrated with buffers (Merck, titrisol) and recalibrated at least every 48 h. The pH of the suspension was continuously adjusted to 6.5 ($\pm$0.05) by software-controlled additions of small volumes of acid (0.1 M HNO_3, 0.3 M $NaNO_3$) or base (0.02 M NaOH, 0.28 M $NaNO_3$) solutions.

The sorption experiment was conducted at 25 $\pm$ 0.1°C in a

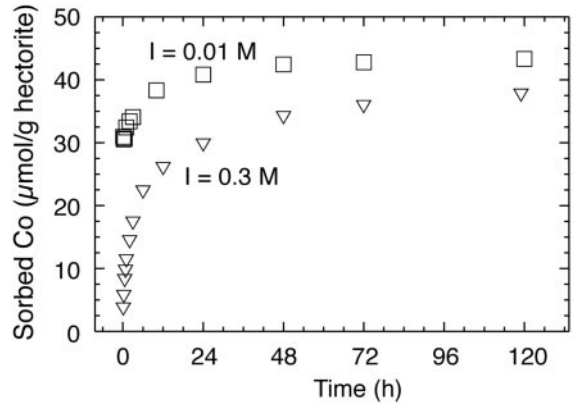

FIG. 5. Kinetics of Co sorption on hectorite at high (I = 0.3 M, ▽) and low (I = 0.01 M, □) ionic strengths. Chemical conditions are: pH 6.5, solid concentration [hectorite] = 1.95 g L^{-1}, total Co concentration $[Co]_{tot}$ = 100 μM.

polyethylene vessel immersed in a thermostated water bath. Solid concentration in the suspension was 1.95 g L^{-1}. Vigorous stirring of the suspension was achieved by a rotating magnetic bar. An inert atmosphere was maintained by bubbling argon throughout the suspension. Prior to use, Ar was acid- and base-washed by bubbling through 10% H_2SO_4 and 0.1 M NaOH solutions, and bubbled through a 0.3 M $NaNO_3$ solution to ensure a constant P_{H_2O} partial pressure. After a preequilibration time of 48 h at pH 6.5, an aliquot of a 0.21 M $Co(NO_3)_2$, 10^{-3} M HNO_3, 0.3 M $NaNO_3$ solution was added to the clay suspension to obtain a final Co concentration of 100 μM. The pH of the suspension was then readjusted to 6.5 within 5 min by gentle addition of the base solution and kept at this value until the end of the experiment. At the end of the sorption period (120 h), Co and Si concentrations in the supernatant were measured by spectrophotometry (38), and Mg was analyzed by inductively coupled plasma-atomic emission spectrometry. The amount of Co sorbed on hectorite at the end of the experiment was equal to 37 μmol g^{-1} of hectorite, i.e. a weight concentration of 2.23×10^{-3} g g^{-1} of hectorite. The free Si concentration in solution amounted to 333 μM at the time of Co introduction in the suspension, and reached a concentration of 394 μM at the end of the sorption period. Dissolved Si was always undersaturated with respect to amorphous silica (solubility of $\sim$2000 μM (39)), and supersaturated with respect to quartz (solubility of 183 μM (40)). This supersaturation can be neglected, owing to the very slow crystallization rate of quartz at room temperature (41).

A 60-μm thick self-supporting film of Co-sorbed hectorite was prepared by slowly filtering 60 mL of the suspension on a 0.05-μm Sartorius cellulose nitrate filter in a closed filtration vessel. In order to avoid atmospheric carbonate contamination, a continuous flow of humidified argon was maintained over the sample throughout the whole filtration stage. Excess of salt and aqueous Co were washed with a few milliliters of Milli-Q water. When dry enough, the thin film was moved into a desiccator. This last drying stage is not believed to have substantially modified the sorption mode of Co, as hectorite is known to retain at least two layers of water molecules, even under low pressure of water vapor (42). Seven slices of the same film were cut and stacked on a sample holder, in order to get a thick sample for fluorescence-yield EXAFS measurements. Upon stacking, these slices were successively rotated around an axis perpendicular to the film plane to ensure a completely random in-plane orientation of hectorite crystallites in the EXAFS sample. The concentration of Co in the sample was low enough ($\Delta\mu/\mu < 0.01$ at $\alpha = 60°$) to eliminate self-absorption effects (43, 44).

Synthesis of Reference Compounds

CoKer of formula $Co_3Si_4O_{10}(OH)_2$, and Co-doped Mg-rich kerolite (CoMgKer) of formula $Co_{0.03}Mg_{2.97}Si_4O_{10}(OH)_2$ were synthesized by aging fresh precipitate of the desired chemical compositions at 75°C for 15 days, according to the procedure described by Decarreau (45, 46). Their b unit cell parameters, as calculated from the position of the (060) diffraction peak, equal 9.30 Å and 9.24 Å, respectively. In these precipitates, Co is located within the phyllosilicate octahedral sheet, and is surrounded by 6 Co and 4 Si (CoKer), or 6 Mg and 4 Si (CoMgKer), respectively. $Co(OH)_{2(s)}$ was obtained by titrating a 0.05 M $Co(NO_3)_2$ solution with 0.2 M NaOH under an argon atmosphere. The fresh pink precipitate was allowed to age for 15 days at room temperature in an anoxic glove box. These reference compounds were loaded in sample holders sealed with Kapton windows for EXAFS measurements.

Quantitative Texture Analysis

QTA was carried out by X-ray diffraction experiments on a four-circle goniometer mounted on a rotating copper anode (Rikagu RU 300-E). The X-ray incident beam was monochromatized using a flat graphite monochromator and collimated, giving a final beam cross section of 1*1 mm^2. Pole densities were measured on a single portion of the hectorite film by scanning the tilt angle ρ between 0 and 85° and the azimuthal angle γ between 0 and 360° with angle increments $\Delta\rho$ and $\Delta\gamma$ of 5°. In order to minimize defocusing effects, relatively open (4 mm) detecting slits were used. Three pole figures were measured: {004}, {020/110}, and {200/130}. Data were corrected for background defocusing. The pole densities were normalized and the OD was refined using the WIMV algorithm (47) of BEARTEX (28). The reflection overlaps are not the exact ones from a theoretical random powder, because defocusing limits the pole figure extent accessible to measurements (ρ only up to 85°). Thus all overlaps were considered as unknowns and were resolved during the OD refinement procedure. The OD was iteratively refined up to a velocity of convergence of 0.3%. Multiple and single pole densities were then recalculated. Visual evaluation of the OD simulation was allowed by comparison of experimental and recalculated pole figures, whereas the quality of the OD refinement was quantified by *RP* and R_W values (26).

EXAFS Data Collection and Reduction

Polarized Co K-EXAFS spectra for the Co-sorbed hectorite film were recorded at the SRS synchrotron radiation facility in Daresbury, UK, on the EXAFS 8.1 station. The optic of the spectrometer consists of a Si(111) double crystal monochromator and a focusing mirror (48). The second crystal of the monochromator was detuned by 30% to increase the rejection rate of harmonics. The clay film was mounted on a goniometer, and EXAFS spectra were recorded at $\alpha = 0°$, 35°, 50°, and 60° in fluorescence detection mode using a 13-element array Ge detector (Canberra).

EXAFS spectra for $Co(OH)_{2(s)}$ and CoKer were recorded in transmission mode at the LURE synchrotron radiation facility, France, on the D42 station, with the plane of the

TABLE 1
Quantitative EXAFS Analysis for Reference Compounds

	First peak						Second peak											
		Co–O shell					Co–Co shell				Co–Mg shell			Co–Si shell				
	IFT range[a] (Å)	R (Å)	N	σ (Å)	R_p	IFT range[a] (Å)	R (Å)	N	σ (Å)	R (Å)	N	σ (Å)	R (Å)	N	σ (Å)	R_P	ΔE_0^b (eV)
$Co(OH)_{2(s)}$	1.1–2.2	2.10	6.0[c]	0.08	0.003	2.2–3.5	3.19[d]	6.0[c]	0.08							0.008	−0.1
CoKer	0.9–2.2	2.09	6.0[c]	0.09	0.012	2.3–3.5	3.12[e]	6.0[c]	0.09				3.27	4.0[c]	0.09	0.003	−0.8
CoMgKer	0.9–2.2	2.08	6.0[c]	0.09	0.005	2.2–3.1				3.07	6.0[c]	0.09	3.21	4.0[c]	0.10	0.035	−0.7

[a] Ranges for inverse Fourier transforms (IFT) in the real space.
[b] The threshold energy E_0 was taken at the half-height of the absorption edge ($\Delta\mu/2$). ΔE_0 given here for FEFF7.02 theoretical functions.
[c] Value held fixed during the fitting procedure.
[d] Crystallographic R_{Co-Co} = 3.17 Å (56).
[e] Crystallographic R_{Co-Co} = 3.10 Å (calculated from the position of the (060) diffraction peak).

sample holder positioned at the magic angle to get rid of any textural effect (24). Measurements were performed using a Si(331) channel-cut monochromator, and gaz ionization chambers filled with an air–helium mixture dosed to attenuate the beam intensity by ~20% before and ~50% after the sample entry. The EXAFS spectrum for CoMgKer was recorded in fluorescence mode at ESRF, France, on the BM32 CRG/IF station. Measurements were performed using a Ni-coated focusing mirror, a Si(111) monochromator, and a 30-element array Ge detector, with the plane of the sample positioned at the magic angle.

EXAFS data reduction was accomplished following a standard procedure (22), using a software package implemented by D. Bonnin (ESPCI, Paris). As a preliminary step, absorption spectra were given the shape of the semi-empirical model of Lengeler (49, 50). $\chi(k)$ for $\alpha = 90°$ was extrapolated from $0° \leq \alpha \leq 60°$ measurements following Eq. [4] (23, 26). Fourier transformation was performed on $k^3\chi(k)$ between 2 and 10 $Å^{-1}$ using a Kaiser apodization window (51), resulting in a radial structure function (RSF) in the distance space. RSF peaks are located at apparent distances ($R + \Delta R$), which differ from crystallographic absorber-backscatterer distances (R) by ~ −0.3 Å, owing to the existence of the phase shift term $\phi_{ij}(k)$ in the EXAFS formula (Eq. [5]) (22). RSF's structural peaks of interest were selected in the distance space, and Fourier-back-transformed in k space. Interatomic distances (R) and number of atomic neighbors (N) were determined by least-square fitting these Fourier-filtered contributions with theoretical phase and amplitude functions calculated with FEFF7.02 (52), using talc, hectorite (Co–Mg and Co–Si pairs) and $Co(OH)_{2(s)}$ (Co–O and Co–Co pairs) as model structures (53–56). The amplitude reduction factor S_0^2 was set to 0.85, in accordance with previous experimental studies (57). The goodness of the fit was quantified by the reliability factor R_P, defined as

$$R_p = \frac{\sum_k (k^3 \cdot \chi_{calc}(k) - k^3 \cdot \chi_{exp}(k))^2}{\sum_k (k^3 \cdot \chi_{exp}(k))^2}. \quad [12]$$

The accuracy of the interatomic distances obtained by using theoretical FEFF functions was assessed by fitting the experimental contributions of the first and second atomic shells for $Co(OH)_{2(s)}$, CoKer and CoMgKer references. Examination of Table 1 shows that EXAFS R_{Co-O} values for the first oxygen shell of the three references are very similar to crystallographic values for divalent and oxygen-hexacoordinated Co (e.g., R_{Co-O} = 2.097 Å for $Co(OH)_{2(s)}$ (56)). EXAFS-derived R_{Co-Co} values for $Co(OH)_{2(s)}$ (3.19 Å) and CoKer (3.12 Å) are both larger than crystallographic distances (3.17 and 3.10 Å, respectively; Table 1). The same difference of 0.02 Å was previously reported (58) and likely originates from uncertainty in theoretical phase shift functions. The EXAFS-derived R_{Co-Mg} value for CoMgKer (3.07 Å) is similar to crystallographic R_{Mg-Mg} distances in talc (3.05–3.06 Å (53)) and to the distance calculated from the b unit cell parameter of CoMgKer (=9.24/3 = 3.08 Å). Finally, EXAFS-derived R_{Co-Si} for CoMgKer (3.21 Å) is lower by 0.03 Å than R_{Mg-Si} in talc (3.24 Å (53)). This result is surprising, as the Co octahedra have a larger size (e.g., R_{Co-O} = 2.097 Å in $Co(OH)_{2(s)}$), compared to Mg octahedra ($R_{Mg-O} \approx$ 2.05–2.08 Å in talc), which should cause Si tetrahedra to be repelled at higher distances. This relatively large uncertainty on R_{Co-Si} cannot be attributed to the use of theoretical FEFF functions (26), but rather results from the overlap of the Mg and Si shells in powder-EXAFS spectra (21, 59). In conclusion, the uncertainty on EXAFS-derived distances resulting from the use of theoretical phase shift functions is about 0.01 Å for Co–O pairs, probably about 0.02 Å for Co–Co and Co–Mg pairs. The uncertainty in distance for Co–Si pairs cannot be estimated with accuracy on powder samples but has been shown to be as good as 0.03 Å in former P-EXAFS experiments (26). The uncertainty on the number of neighboring atoms will be discussed later.

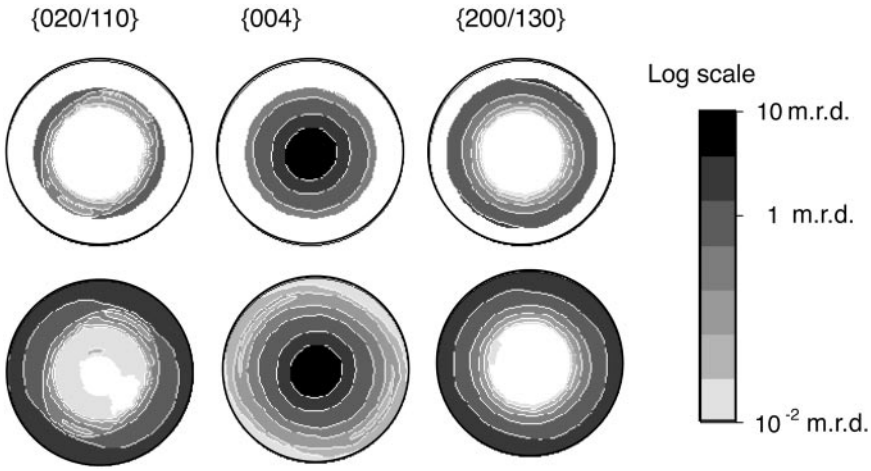

FIG. 6. Normalized, experimental (above) and recalculated (below) pole figures for Co-sorbed hectorite (logarithmic density scale, equal area projection). Note that experimental pole figures are satisfactorily reproduced by the computation.

RESULTS AND INTERPRETATION

Texture Analysis

Normalized experimental and OD-recalculated pole figures are presented in Fig. 6. Pole densities are expressed in multiple of a random distribution (m.r.d.). Experimental and recalculated patterns look similar to each other, with low (i.e., good) reliability factors. Reliability factors for density values above 1 m.r.d. of $RP_1 = 2.3\%$, and for all densities of $RP_0 = 5\%$, were obtained at the end of the refinement. The corresponding weighted factors are $R_{W1} = 1.4\%$ and $R_{W0} = 6.1\%$ (26).

Zones of iso-densities form nonconstant rings on the {020/110} pole figure and to some extent on the {200/130} pole figure as well. One would see in such density variations an effect of preferential orientations of **a** and **b** axes in the film plane. However, these irregularities affect only the peripheral part of each pole figure, where the beam may not hit regularly the sample, and are located at the same azimuthal angle for all pole figures. This observation is not consistent with a texture effect for different {*hkl*} reflections; we therefore conclude to a geometrical effect due to a nonregular irradiation of the sample during γ rotation. Thus, it can be concluded that **a** and **b** axes of crystallites are randomly distributed in the film plane. This observation, combined with the high density at the center of the {004} pole figure, indicates that the distribution of crystallites in the thin film is axisymmetrical, or, in other words, that a C_∞ symmetry axis exists perpendicular to the film plane. The presence of this axisymmetry indicates that it is possible to apply Eqs. [4] and [7]–[11]. Manceau *et al.* (26) drew the same conclusion on a self-supporting film of nontronite.

Figure 7a represents the {001} distribution recalculated from the OD. This reflection has a maximum orientation density of 11 m.r.d., which is an indication of a highly textured film, but is lower than the value of 39 m.r.d. reported for a nontronite self-supporting film (26). The difference of texture strength of the two films possibly originates from the greater thickness of the hectorite film (~60 μm) as compared to that of nontronite (~20 μm). The increase in thickness allowed us to increase the intensity of the fluorescence signal during EXAFS acquisition.

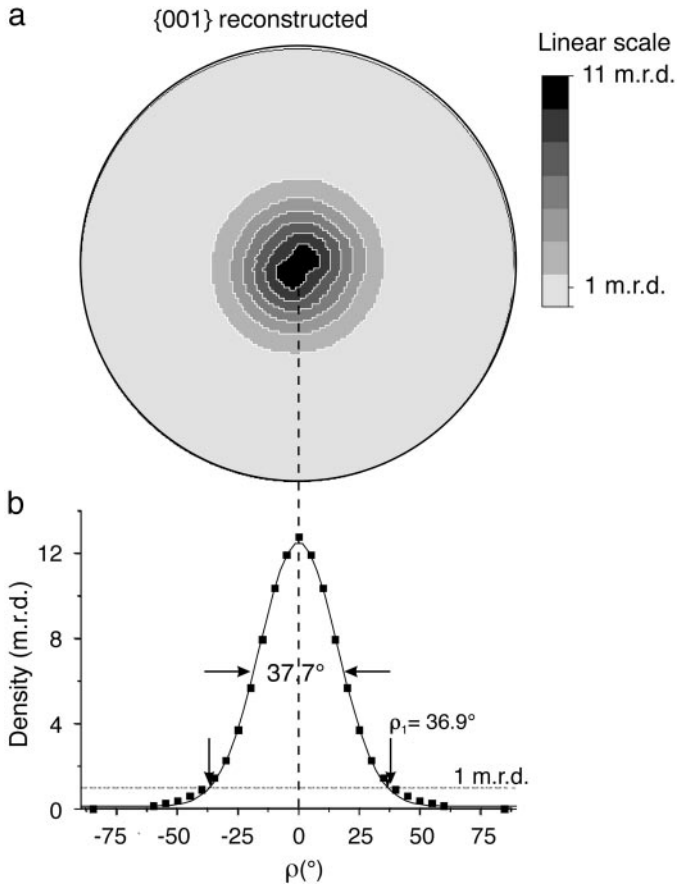

FIG. 7. (a) Recalculated {001} pole figure for hectorite (linear density scale, equal area projection). (b) Integrated ρ scan of the {001} pole figure. The 1 m.r.d. density is represented by an horizontal dashed line and the gaussian fit to the ρ scan by a solid line.

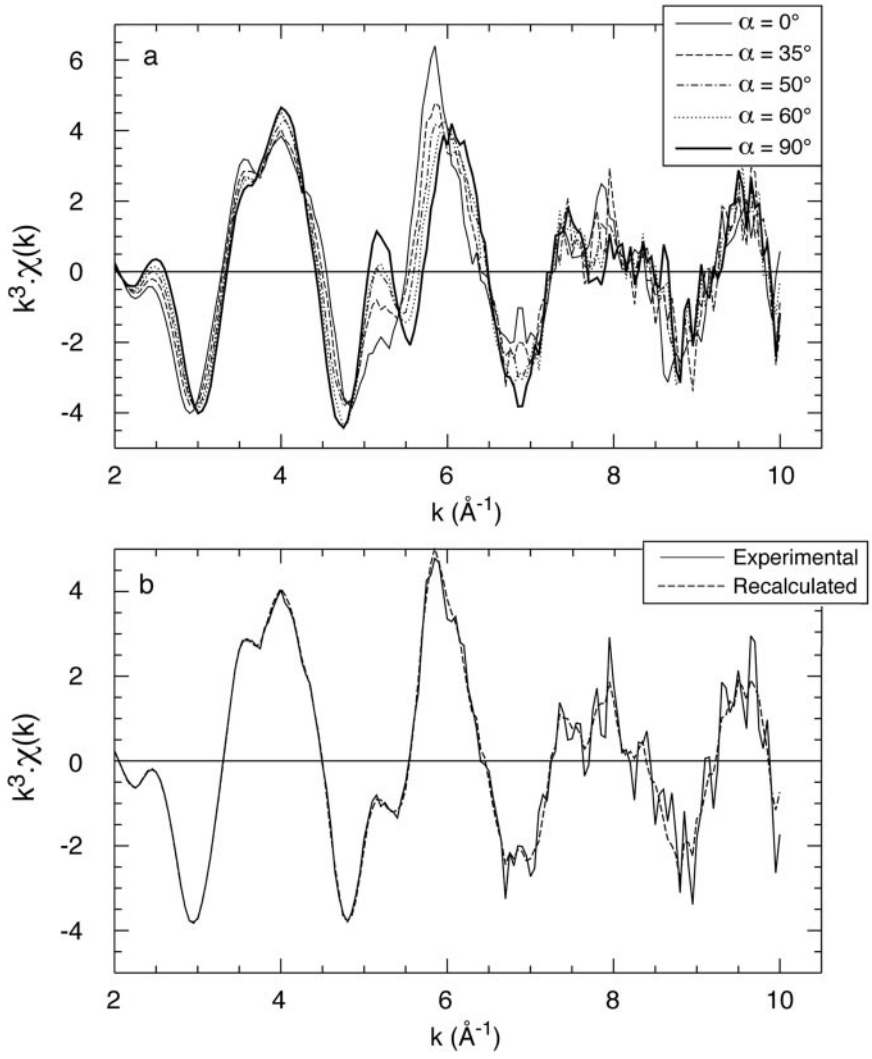

FIG. 8. (a) k^3-weighted Co K-edge EXAFS spectra at α angles of 0°, 35°, 50°, 60°, and 90°. The 90° spectrum has been obtained by regression of the experimental data for $0 \leq \alpha \leq 60°$ and extrapolation to $\alpha = 90°$. (b) Comparison of the experimental (solid line) and extrapolated-recalculated (dashed line) k^3-weighted EXAFS spectra for $\alpha = 35°$.

A ρ-transect of the {001} density distribution was obtained by averaging for each ρ value the normalized densities of the {001} pole figure over all γ angles (Fig. 7b). The dispersion of **c*** axes of individual platelets off the film normal can be quantified by the full width at half maximum (FWHM) of this ρ-transect. Here the FWHM is equal to 37.7°, as compared to 19.8° for Garfield nontronite (26). This lower orientation is expected to diminish slightly the angular dependence of P-EXAFS spectra. The difference between N_j^{app} obtained for an ideal texture (Eq. [10]) and the value obtained for real samples (N_j^{exp}) was calculated by Manceau *et al.* (25) in the case of a step-shaped distribution of **c*** axis symmetrically around the film normal. These calculations showed that for a distribution having a step-shaped width of 40°, $(N_j^{app} - N_j^{exp})/N_j^{app}$ is equal to 11% at $\alpha = 90°$ for $\beta = 33°$, and equals 4% at $\alpha = 0°$ for $\beta = 90°$. Consequently, N_j^{exp} can be considered equal to N_j^{app} as a first approximation.

EXAFS Spectra

The EXAFS spectra recorded at different α angles and the extrapolated spectrum at $\alpha = 90°$ are displayed in Fig. 8a. The quality of the extrapolation procedure was estimated by comparing the experimental spectrum at $\alpha = 35°$, $\chi_{exp}^{35°}(k)$ to that recalculated from the regression procedure, $\chi_{calc}^{35°}(k)$ (Fig. 8b). The agreement between these two spectra is very good at low k and decreases at high k, as a result of the increase of the signal to noise ratio. Close examination of Fig. 8b shows that $\chi_{calc}^{35°}(k)$ is less noisy than $\chi_{exp}^{35°}(k)$, especially at high k. One can see in this observation an effect of the calculation of $\chi_{calc}^{35°}(k)$ via linear regression of independent experimental points. This in-

ference can be checked by comparing the uncertainty of the measurements for $\chi^{35^\circ}_{exp}(k)$ ($s^{\alpha}_{exp}(k)$) and for $\chi^{35^\circ}_{calc}(k)$ ($s^{\alpha}_{calc}(k)$) with the assumption that $s^{\alpha}_{exp}(k)$ is independent on α, i.e. that $s_{exp}(k)$ is the same for all experimental spectra; $s_{exp}(k)$ and $s^{\alpha}_{calc}(k)$ are then related by (60)

$$s^{\alpha}_{calc} = s_{exp}(k) \cdot \left[\frac{1}{n} + \frac{(\cos^2\alpha_{calc} - \langle \cos^2\alpha_{exp} \rangle)^2}{\sum_{\alpha_{exp}} (\cos^2\alpha_{exp} - \langle \cos^2\alpha_{exp} \rangle)^2} \right]^{1/2}, \quad [13]$$

where α_{exp} is the experimental angle ($\alpha_{exp} = 0°$, 35°, 50°, and 60°), n is the number of experimental spectra (here $n = 4$), and α_{calc} is the angle of the calculated spectrum. Application of Eq. [13] results in $s^{35^\circ}_{calc}(k) = 0.52 * s_{exp}(k)$, which means that the recalculated spectrum is theoretically about half as noisy as the experimental one. This calculation compares favorably with the reduction of noise observed for $\chi^{35^\circ}_{calc}(k)$ (Fig. 8b). Furthermore, for $\alpha = 90°$, $s^{90^\circ}_{calc}(k) = 1.14 * s_{exp}(k)$, which suggests that $\chi^{90^\circ}_{calc}(k)$ has a similar signal to noise ratio as the experimental spectra. This result allows us to place confidence in the regression and calculation procedure.

P-EXAFS spectra (Fig. 8a) contain several distinct frequencies having a large amplitude, even at high k. Multiple scattering paths do not have a large amplitude at high k. Hence, the observed multifrequency indicates the presence of several backscattering shells around Co. The position and amplitude of several oscillation maxima vary as a function of α. For example, the maximum centered near 6 $Å^{-1}$ ($\alpha = 0°$) shifts to higher k with increasing α, whereas the opposite trend is observed for the maximum near 4.2 $Å^{-1}$. These modifications cannot be interpreted by the variation of a hypothetical self-absorption effect with α, as this effect solely modifies the amplitude of $\chi^{\alpha}(k)$ (43, 61), and also because of the low concentration of Co within the sample ($\Delta\mu/\mu < 0.01$). Instead, these angular variations originate from a polarization dependence of the EXAFS contributions. It has been seen in the background section that the amplitude of the contribution of an atomic j shell (χ_{Co-j}) depends on its β_j angle. Therefore, the occurrence of multiple wave frequencies, together with the polarization dependence of EXAFS spectra, indicate that Co atoms are surrounded by several atomic shells oriented differently with respect to **c***. The angular dependence of EXAFS spectra also suggests that sorbed Co atoms are associated structurally to hectorite platelets.

EXAFS spectra recorded at the magic angle for Co-sorbed hectorite and reference compounds are contrasted in Fig. 9. Co-sorbed hectorite has a markedly different EXAFS spectrum from CoKer and $Co(OH)_{2(s)}$, which points to distinct crystallochemical environments. This simple comparison indicates that sorbed Co did not precipitate as pure $Co(OH)_{2(s)}$ or CoKer, as expected from the careful choice of sorption chemical conditions. Instead, EXAFS spectra of Co-sorbed hectorite and CoMgKer bear strong similarities, which suggests that sorbed Co is located, at least partially, in a Mg clay-like environment.

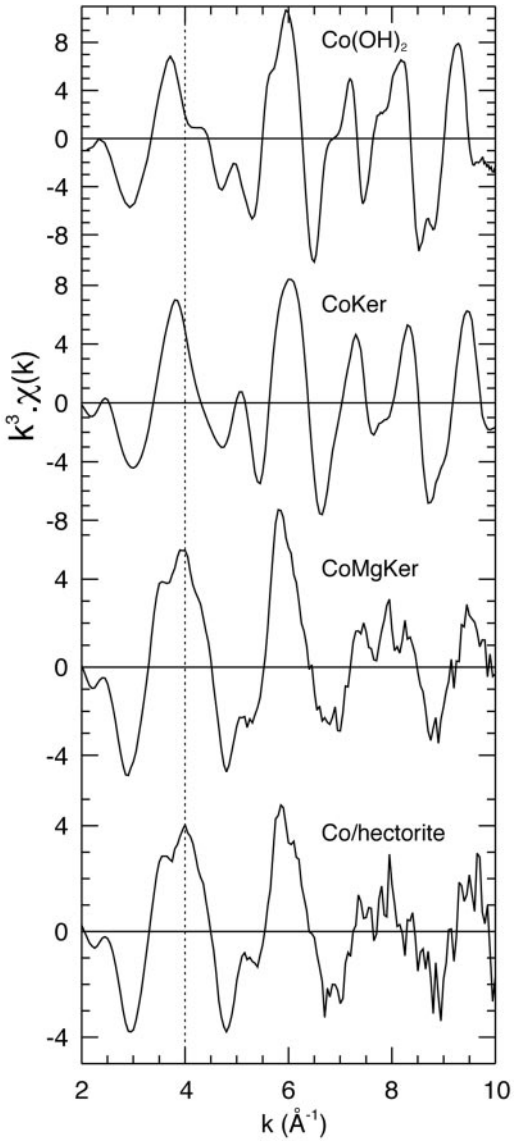

FIG. 9. k^3-weighted Co K-edge EXAFS spectra for $Co(OH)_{2(s)}$, Co-rich kerolite (CoKer), Co-doped Mg-rich kerolite (CoMgKer), and Co-sorbed hectorite. All spectra were recorded at the magic angle.

Radial Structure Functions (RSFs)

RSFs corresponding to the P-EXAFS spectra in Fig. 8a are plotted in Fig. 10. Several intense peaks are observed at $R + \Delta R$ distances of 1.8 Å and 2.7–2.8 Å. These peaks point to the presence of several atomic shells in the vicinity of sorbed Co, which is fully consistent with the occurrence of several wave frequencies noted previously in P-EXAFS spectra. Figure 11 shows that the RSFs of $Co(OH)_{2(s)}$, CoKer, and Co-sorbed hectorite at $\alpha = 35°$ differ by the position and amplitude of their second structural peaks, which confirms that Co has a different structural environment in Co-sorbed hectorite and in these references. A significant difference of amplitude can also be observed between Co-sorbed hectorite and CoMgKer,

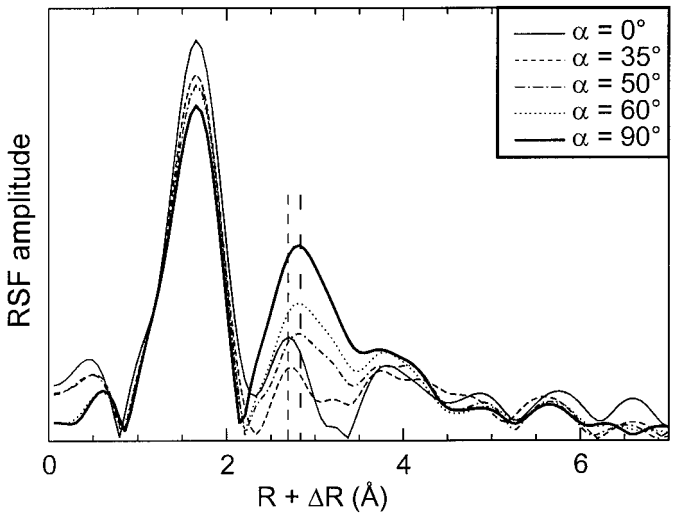

FIG. 10. Polarization dependence of the Co K-edge RSF for Co-sorbed hectorite at α angles of 0°, 35°, 50°, 60° (experimental), and 90° (extrapolated).

which suggests that either the number or the nature of neighboring cations are different in these two compounds.

First RSF Peak

The first RSF peak at $R + \Delta R = 1.8$ Å corresponds to the contribution of oxygen atoms coordinated to Co. The R_{Co-O} distance was determined by least-squares fitting the partial EXAFS contribution obtained by Fourier back-transforming this RSF peak. Good fits ($R_P \leq 0.006$ for $0° \leq \alpha \leq 60°$, and $R_P = 0.010$ for $\alpha = 90°$) were obtained by assuming 5.6 ($\alpha = 0°$) to 4.3 ($\alpha = 90°$) oxygen atoms at $R_{Co-O} = 2.08$ Å ($\sigma = 0.10$ Å) (Table 2). The uncertainty on R_{Co-O} and N_O resulting from experimental measurements and spectral analysis were estimated at $\alpha = 35°$ by successively varying and fixing these structural parameters during the least-squares fit. A 0.02 Å shift of R_{Co-O} from its best-fit value, or an increase of N_O from 5.1 to 6 (20%), led to a two-time increase of R_P. However, this estimation procedure does not take into account the possible offset of R_{Co-O} resulting from the use of theoretical phase shift functions. This R_{Co-O} offset was previously inferred to 0.01 Å from the analysis of references. Therefore, the experimental uncertainty on R_{Co-O} and N_O are typically ± 0.03 Å and $\pm 20\%$, respectively.

The value of R_{Co-O} confirms that sorbed Co is divalent and hexacoordinated to oxygen (62), as fourfold coordinated Co or sixfold coordinated Co(III) would have resulted in shorter Co–O distances of 1.9–2.0 Å. It can therefore be concluded that no redox reaction occurred during the sample preparation. The relatively high value of σ ($\sigma = 0.10$ Å), and the low number of detected oxygens ($4.3 \leq N_O \leq 5.6$), in comparison to CoKer and $Co(OH)_{2(s)}$, point to an increase in the dispersion of Co–O bond lengths in the sorption sample. The larger spread of R_{Co-O} likely results from difference of bond strengths, possibly because oxygens coordinated to Co belong to distinct chemical entities, such as H_2O molecules, OH groups, and oxygens of the sorbent surface. This structural disorder causes a damping of the EXAFS signal, which is not fully compensated by an increase of σ, so that the number of oxygens detected by EXAFS is lower than the actual number coordinated to Co. Since this difference between the detected and the actual number of oxygens is structural in origin, it was not taken into account in the previous estimate of the experimental uncertainty. Therefore, the real uncertainty on N_O, which sums up the experimental uncertainty and the effects of structural disorder, is probably higher than 20%.

The amplitude of first RSF peaks decreases with increasing α (Fig. 10), and this lowering is reflected in Table 2 by a reduction of N_O^{app} from 5.6 at $\alpha = 0°$ to 4.3 at $\alpha = 90°$. As exposed in the background section, the sense of this variation indicates that $\beta_O > 54.7°$, i.e. that the coordination octahedron is flattened (26). To quantify this flattening, β_O has been estimated as follows. First, a linear regression of N_O^{app} with respect to $\cos^2\alpha$ was performed for $0° \leq \alpha \leq 60°$ (Fig. 12). Second, $N_O^{real} = 5.18$ was calculated from this regression equation at the magic angle $\alpha = 35.3°$. Third, application of Eq.

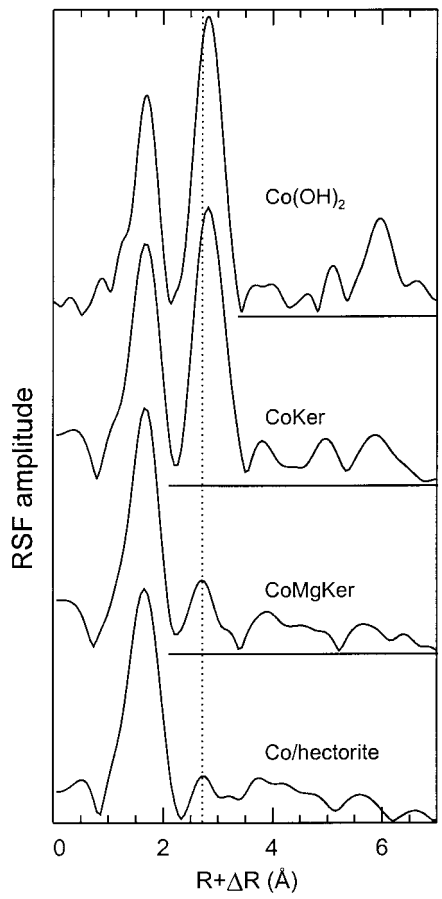

FIG. 11. Co K-edge RSF for $Co(OH)_{2(s)}$, Co-rich kerolite (CoKer), Co-doped Mg-rich kerolite (CoMgKer), and Co-sorbed hectorite.

TABLE 2
Quantitative EXAFS Analysis for Co-Sorbed Hectorite

	First peak					Second peak								
		Co–O shell					Co–Mg shell			Co–Si shell				
α	IFT range[b] (Å)	R (Å)	N_O^{app}	σ (Å)	R_p	IFT range[b] (Å)	R (Å)	N_{Mg}^{app}	σ (Å)	R (Å)	N_{Si}^{app}	σ (Å)	R_P	ΔE_0^a (eV)
0°	0.9–2.2	2.08[c]	5.6	0.10[c]	0.004	2.3–3.3	3.03	2.3	0.10[c]	3.27[c]	0.5	0.11[c]	0.022	−0.1
35°	0.9–2.2	2.08	5.1	0.10	0.002	2.3–3.3	3.03[c]	1.6	0.10[c]	3.27[c]	2.2	0.11[c]	0.015	−0.1
50°	0.9–2.2	2.08[c]	4.9	0.10[c]	0.005	2.2–3.3	3.03[c]	1.1	0.10[c]	3.27[c]	3.6	0.11[c]	0.031	−0.1
60°	0.9–2.2	2.08[c]	4.7	0.10[c]	0.006	2.2–3.4	3.03[c]	0.6	0.10[c]	3.27[c]	4.4	0.11[c]	0.029	−0.1
90°	0.9–2.2	2.08[c]	4.35	0.10[c]	0.010	2.2–3.4				3.27	5.8	0.11	0.029	−0.1

[a] The threshold energy E_0 was taken at the half-height of the absorption edge ($\Delta\mu/2$). ΔE_0 given here for FEFF7.02 theoretical functions.
[b] Ranges for inverse Fourier transforms (IFT) in the real space.
[c] Value held fixed during the fitting procedure.

[11] with $N_O^{real} = 5.18$ yielded $\beta_O^{exp} = 57.9°$. The statistical uncertainty on β_O^{exp} was obtained from the dispersion of N_O^{app} off the regression line (60) and was equal to $\pm 1°$ at the 95.5% confidence level. As discussed in the background section, the real β_O value (β_O^{real}) is probably slightly higher than the experimental β_O^{exp} value, because of the disorientation of individual platelets off the film plane. Nevertheless, β_O^{exp} compares well with β_O for edge-sharing octahedra in Co-substituted synthetic mica (~58.2° (63)).

Second RSF Peak

The high amplitude of the RSF peak near $R + \Delta R = 2.7$–2.8 Å for $\alpha = 0°$ and 90° suggests that it originates from the contribution of nearest cationic shells, which may consist of either Co, Si, or Mg. This peak displays a complex angular dependence, decreasing from $\alpha = 0°$ to $\alpha = 35°$, and then increasing from $\alpha = 35°$ to $\alpha = 90°$. Meantime, its maximum shifts from $R + \Delta R = 2.7$ Å to 2.8 Å as α increases. If this peak arised from a *single* atomic shell contribution, then its position would be invariant with α (Eq. [8]). Therefore, the shift in position with α indicates that this peak is made of the contributions of at least two atomic subshells, consisting either of chemically identical atoms located at different distances from Co, or of chemically different atoms. Furthermore, this angular effect can only be observed if the contribution of one subshell predominates at $\alpha = 0°$ and the other at $\alpha = 90°$, i.e., if these two subshells have different β_j angles.

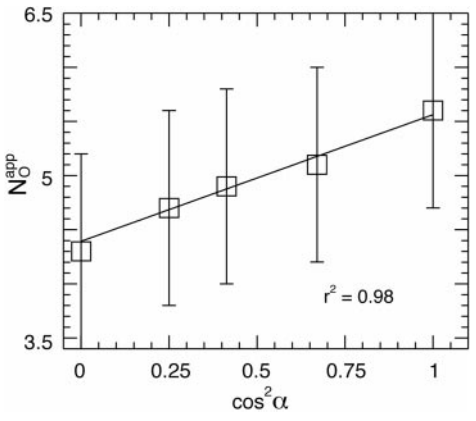

FIG. 12. Angular dependence of the apparent number of oxygen neighbors (N_O^{app}) for Co-sorbed hectorite. Squares: experimental data. Linear regression of experimental data (solid line) for $0 \le \alpha \le 60°$ yielded $N_O^{app} = 1.17*\cos^2\alpha + 4.39$.

Back-Fourier transforms of second RSF peaks for $\alpha = 0°$, 35°, and 90° are contrasted in Fig. 13a. Of significance is the presence of isosbestic points, for which χ_{ij}^P is independent of α. These points are much sensitive to defaults in spectral normalization, and their observation over the entire k-span attests for the reliability of the data analysis. This reliability can be further assessed by comparing the experimental $\chi_{2nd\,peak}^{35°}$ contribution to that recalculated from $\chi_{2nd\,peak}^{0°}$ and $\chi_{2nd\,peak}^{90°}$ by the theoretical expression derived from Eq. [4],

$$\chi_{2nd\,peak}^{35°} = \tfrac{2}{3} \cdot \chi_{2nd\,peak}^{0°} + \tfrac{1}{3} \cdot \chi_{2nd\,peak}^{90°}. \qquad [14]$$

Figure 13b shows that experimental and recalculated $\chi_{2nd\,peak}^{35°}$ are hardly distinguishable. This very good quantitative agreement ($R_P = 8 \times 10^{-3}$) deserves to be emphasized and denotes the fair precision of measurements in the $3 \le k \le 10$ Å^{-1} interval.

Chemical nature of the predominant contributions at $\alpha = 0°$ and 90°. That the second shell contains at least two subshells whose contributions alternatively predominate at $\alpha = 0°$ and $\alpha = 90°$ has been shown in the previous section. The simplest hypothesis consists of assuming that this second shell comprises *only* two subshells, denoted M1 and M2. According to Eq. [5], the EXAFS contribution of M1 and M2 can be written as a damped sinusoid with a frequency that depends on the absorber-backscatterer distance ($2kR_{ij}$ term), and on the chemical nature of the backscatterer (ϕ_{ij} term). Therefore, the phase

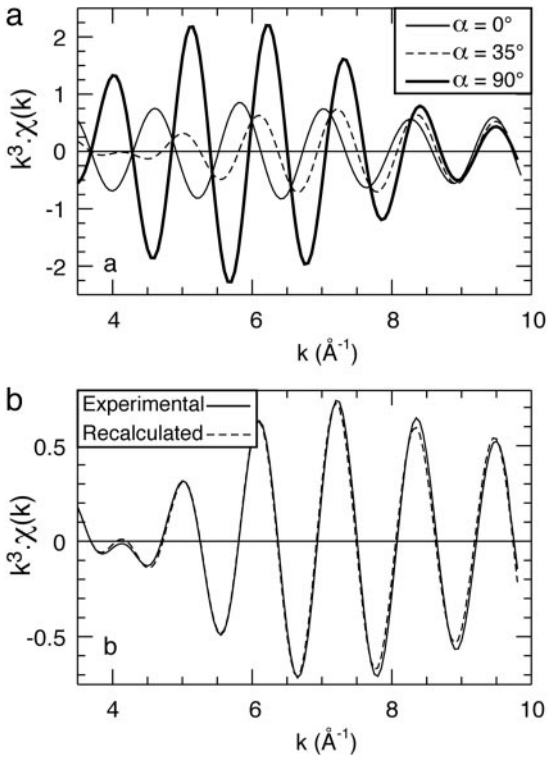

FIG. 13. Fourier-filtered EXAFS spectra of the second shell ($\chi_{\text{2nd shell}}(k)$) for Co-sorbed hectorite. (a) Comparison of $\chi_{\text{2nd shell}}(k)$ for $\alpha = 0°$, 35°, and 90°. (b) Comparison of the experimental $\chi^{35°}_{\text{2nd peak}}$ contribution (solid line) and the $\chi^{35°}_{\text{2nd peak}}$ contribution recalculated from $\chi^{0°}_{\text{2nd peak}}$ and $\chi^{90°}_{\text{2nd peak}}$ (dashed line).

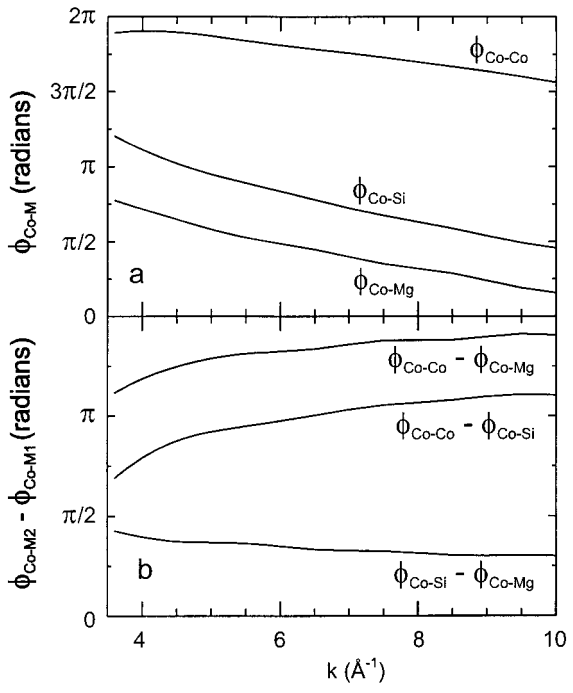

FIG. 14. FEFF7.02 calculated phase shift functions for Co–Co, Co–Si, and Co–Mg pairs and interatomic distances of 3.10 Å. (a) Plot of the phase shift functions. (b) Plot of the difference of phase ($\Delta\varphi$) for various combinations of atomic pairs.

difference between the $\chi_{\text{Co–M1}}(k)$ and $\chi_{\text{Co–M2}}(k)$ waves is given by

$$\begin{aligned}\Delta\varphi(k) &= \varphi_{\text{M2}}(k) - \varphi_{\text{M1}}(k)\\ &= 2k(R_{\text{Co–M2}} - R_{\text{Co–M1}})\\ &\quad + (\phi_{\text{Co–M2}}(k) - \phi_{\text{Co–M1}}(k));\end{aligned} \qquad [15]$$

$\Delta\varphi$ can be estimated experimentally by supposing that $\chi^{0°}_{\text{2nd peak}}$ contains only the contribution of M1 and $\chi^{90°}_{\text{2nd peak}}$ contains only the contribution of M2, so that $\Delta\varphi$ is simply the phase difference between $\chi^{0°}_{\text{2nd peak}}$ and $\chi^{90°}_{\text{2nd peak}}$. This phase difference can be read out on Fig. 13a and equals π at $k = 4$ Å^{-1}, and 2π at $k = 9.5$ Å^{-1}. In the following, M1 and M2 will be identified by their ability to verify Eq. [15] at $k = 4$ and 9.5 Å^{-1}.

Let us first assume that $R_{\text{Co–M2}} = R_{\text{Co–M1}}$ and that the two subshells are chemically different. Equation [15] then reduces to $\Delta\varphi(k) = \phi_{\text{Co–M2}}(k) - \phi_{\text{Co–M1}}(k)$. Theoretical $\Delta\varphi$ functions corresponding to the various combinations of possible M1 and M2 subshells were obtained from $\phi_{\text{Co–Co}}(k)$, $\phi_{\text{Co–Mg}}(k)$ and $\phi_{\text{Co–Si}}(k)$ phase shift functions (Fig. 14a) computed with FEFF7.02. Examination of Fig. 14b shows that none of the $\Delta\varphi$ functions verify $\Delta\varphi = \pi$ at $k = 4$ Å^{-1} and $\Delta\varphi = 2\pi$ at $k = 9.5$ Å^{-1}. Therefore, this hypothesis should be ruled out.

Let us then assume that the two subshells are chemically different and that $R_{\text{Co–M2}} \neq R_{\text{Co–M1}}$. Equation [15] can then be rewritten

$$R_{\text{M2}} - R_{\text{M1}} = \frac{\Delta\varphi - (\phi_{\text{Co–M2}}(k) - \phi_{\text{Co–M1}}(k))}{2k}. \qquad [16]$$

$R_{\text{M2}} - R_{\text{M1}}$ values calculated for the different combinations of atomic pairs are listed in Table 3 for $k = 4$ and 9.5 Å^{-1}. There is no atomic pair for which $R_{\text{M2}} - R_{\text{M1}}$ is completely indepen-

TABLE 3

Calculated Differences of Distance between M1 and M2 Subshells at $k = 4$ and 9.5 Å^{-1} and for Different Combinations of M1 and M2 Subshells

M1	M2	$(R_{\text{M2}} - R_{\text{M1}})$ for $k = 4$ Å^{-1}	$(R_{\text{M2}} - R_{\text{M1}})$ for $k = 9.5$ Å^{-1}	$\Delta(R_{\text{M2}} - R_{\text{M1}})^a$ (Å)
Co	Mg	0.85	0.56	−0.29
Co	Si	0.70	0.51	−0.19
Si	Co	0.08	0.15	0.07
Si	Mg	0.54	0.38	−0.16
Mg	Co	−0.07	0.09	0.16
Mg	Si	0.24	0.28	0.04

[a] Calculated as follows: $\Delta(R_{\text{M2}} - R_{\text{M1}}) = (R_{\text{M2}} - R_{\text{M1}})_{k=9.5\text{Å}^{-1}} - (R_{\text{M2}} - R_{\text{M1}})_{k=4\text{Å}^{-1}}$.

dent of k. This suggests that at least one of the $\chi^{0°}_{\text{2nd peak}}$ or $\chi^{90°}_{\text{2nd peak}}$ functions does not originate from a single subshell. The smallest variation of $R_{M2} - R_{M1}$ from $k = 4$ to $k = 9.5$ Å^{-1} corresponds to M1 = Mg and M2 = Si (Table 3). All other combinations of atomic pairs (including pairs of chemically identical atoms) result in variations of $R_{M2} - R_{M1}$ at least 1.5 times larger. Therefore, this preliminary analysis suggests that predominant backscatterers are Mg at 0° and Si at 90°. The sign of $R_{Si} - R_{Mg}$ indicates that the Si subshell is more distant from Co than the Mg one. The exact nature of the atomic contributions contained in $\chi^{0°}_{\text{2nd peak}}$ and $\chi^{90°}_{\text{2nd peak}}$ will be identified below.

Quantitative analysis. At first, $\chi^{\alpha}_{\text{2nd peak}}(k)$ functions were tentatively fitted by assuming only Mg backscatterers at $\alpha = 0°$ and Si backscatterers at $\alpha = 90°$. Only three parameters (N, R, and σ) were allowed to vary for each shell. This single shell analysis yielded a good fit at $\alpha = 90°$ ($R_P = 0.029$), with $N^{app}_{Si} = 5.8$ and $R_{Co–Si} = 3.27$ Å ($\sigma_{Si} = 0.11$ Å). The agreement was not as good at $\alpha = 0°$ ($R_P = 0.059$), and a two-shell fit was therefore performed with Mg and Si neighbors, by fixing σ_{Si} and $R_{Co–Si}$ to their value at $\alpha = 90°$. A good agreement ($R_P = 0.022$) was obtained with $N^{app}_{Si} = 0.5$, $N^{app}_{Mg} = 2.3$, and $R_{Co–Mg} = 3.03$ Å ($\sigma_{Mg} = 0.10$ Å) (Fig. 15 and Table 2). Finally, $\chi^{\alpha}_{\text{2nd peak}}(k)$ for $35° \leq \alpha \leq 60°$ were fitted by varying only N^{app}_{Mg} and N^{app}_{Si} and fixing σ and R identical to their value at $\alpha = 0°$ and 90° (Fig. 15). The experimental uncertainty on the structural parameters was estimated at $\alpha = 35°$ by varying and fixing successively $R_{Co–Si}$, $R_{Co–Mg}$, N_{Mg}, and N_{Si}. This procedure showed that the figure of merit, R_P, increased from 0.015 to 0.022 and that the spectral fit was visually substantially degraded as N_{Mg} was varied from 1.6 to 2, or from 1.6 to 1.3. Thus, the estimated uncertainty on N^{app}_{Mg} resulting from experimental data collection and analysis is ±0.4 (i.e., 25% of N^{app}_{Mg}). Application of the same procedure to the other adjusted parameters yielded an estimated experimental uncertainty on N^{app}_{Si} of ±0.5 and on (R_{Mg}, R_{Si}) of ±0.02 Å. A small $\chi_{Co–Co}$ component was also introduced during the fit to detect the possible presence of Co polynuclear complexes. The quality of the fit was significantly altered upon the introduction of a Co content as low as 0.1 ($\sigma = 0.11$ Å), leading to an increase of R_P from 0.015 to 0.020, and a shift to high k of the maximum of the $\chi(k)$ envelope (data not shown). This shift can be accounted for by observing that the amplitude of $\chi_{Co–Co}(k)$ (Fig. 15, $Co(OH)_{2(s)}$ reference) peaks at 7–8 Å^{-1}, whereas the amplitude of $\chi^{\alpha}_{\text{2nd peak}}(k)$ peaks at 6 Å^{-1} for Co-sorbed hectorite. Therefore, $N_{Co} = 0.1$ can be taken as an upper limit, which indicates that less than 10% of sorbed Co is present as dimers, or less than 1.8% as a Co precipitate.

Relatively high σ values ($\sigma = 0.10–0.11$ Å) were required to fit $\chi^{\alpha}_{\text{2nd peak}}(k)$ for Co-sorbed hectorite, as compared to reference compounds ($\sigma = 0.09–0.10$ Å). As previously discussed for the oxygen shell, these high σ values are symptomatic of a significant dispersion of interatomic distances, and EXAFS may not be sensitive to their full distribution, yielding a lower number of detected backscatterers than actually present. Since this loss of atomic neighbors is of structural origin, it should be added to the uncertainty coming from data collection and

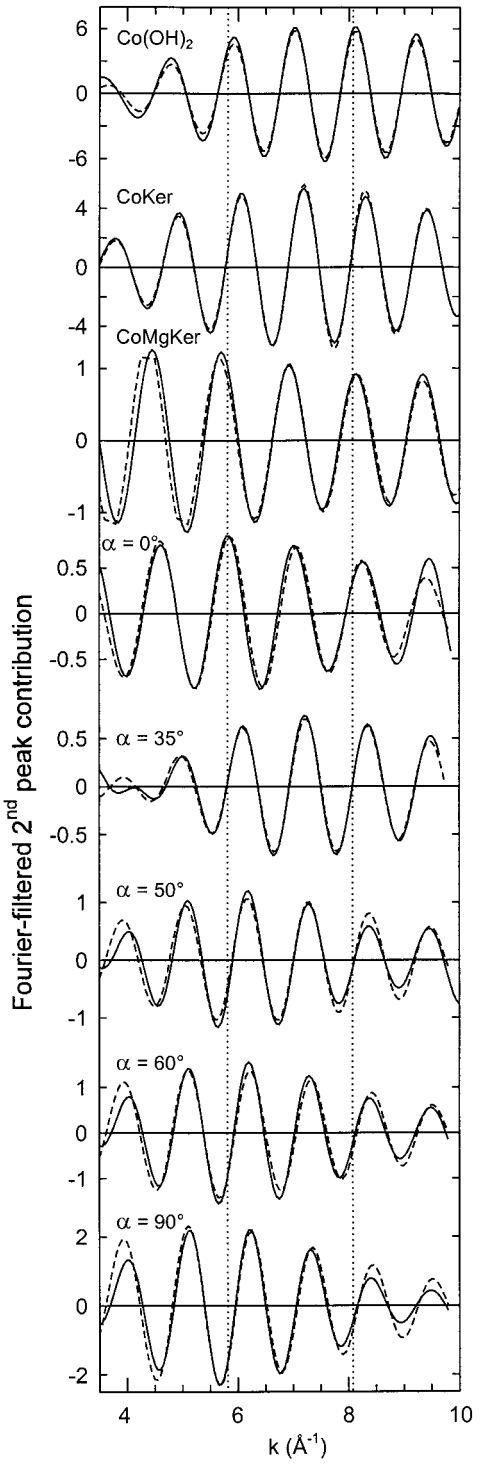

FIG. 15. Comparison between experimental and modeled $\chi_{\text{2nd shell}}(k)$ contributions for $Co(OH)_{2(s)}$, Co-rich kerolite (CoKer), Co-doped Mg-rich kerolite (CoMgKer), and Co-sorbed hectorite from $\alpha = 0°$ to $\alpha = 90°$.

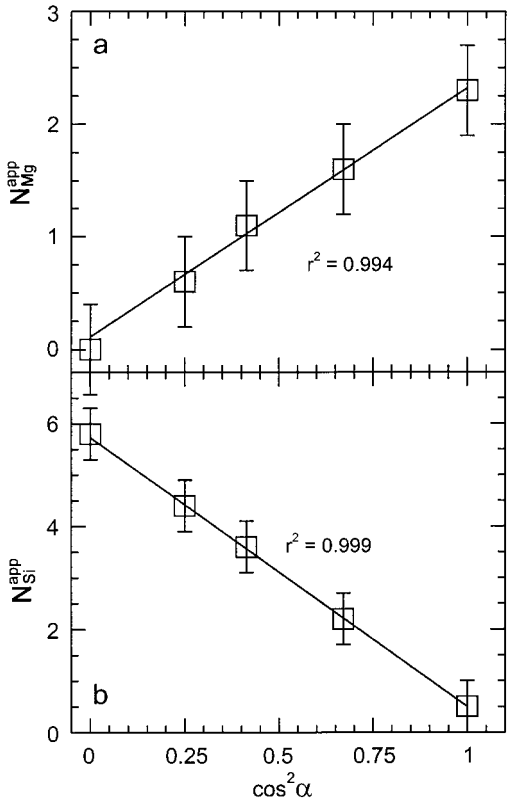

FIG. 16. Angular dependence of the apparent number of nearest Mg (N_{Mg}^{app}) (a) and Si (N_{Si}^{app}) (b) atoms for Co-sorbed hectorite. Squares: experimental data. Linear regression of experimental data for $0 \leq \alpha \leq 60°$ (solid lines) yielded $N_{Mg}^{app} = 2.21*\cos^2\alpha + 0.11$ and $N_{Si}^{app} = -5.22*\cos^2\alpha + 5.72$.

analysis. The total uncertainty on N_{Mg}^{app} and N_{Si}^{app} are thus probably higher than 25%.

N_{Mg}^{app} and N_{Si}^{app} are plotted in Fig. 16 as a function of $\cos^2\alpha$. Good linear correlations between N^{app} and $\cos^2\alpha$ are found for the two subshells, with regression coefficients $r^2 > 0.99$. β_{Mg}^{exp} and β_{Si}^{exp} were calculated in the same way as β_O^{exp}, and the uncertainty on β_{Mg}^{exp} and β_{Si}^{exp} were estimated from the dispersion of N_{Mg}^{app} and N_{Si}^{app} off the regression lines. This calculation yielded $\beta_{Mg}^{exp} = 80.1 \pm 10.2°$, and $\beta_{Si}^{exp} = 22.2° \pm 1.4°$. Consequently, Co–Mg pairs are, to the precision of the method, parallel to the film plane, whereas Co–Si pairs are inclined by ~20° off the normal to this plane.

DISCUSSION

Mechanism of Co Sorption

P-EXAFS showed that the structural environment of Co atoms sorbed on hectorite is highly anisotropic. This structural anisotropy concerns the coordination octahedron of Co, which is flattened, and the second shell, made of in-plane Mg and out-of-plane Si atoms located at $R_{Co–Mg} = 3.03$ Å and $R_{Co–Si} = 3.27$ Å. This structural information will serve to determine the sorption mechanism(s) of Co among the several ones that are consistent with the structural association between the sorbate and the sorbent: (a) outer-sphere surface adsorption, (b) inner-sphere surface adsorption, (c) surface precipitation of $Co(OH)_{2(s)}$ or of phyllosilicate-like compounds, and (d) diffusion within octahedral vacancies of hectorite (64).

In an outer-sphere adsorption mechanism, the sorbate is held in the vicinity of the sorbent surface without loosing its hydration shell. Neighboring cations from the sorbent are then relegated at distances higher than ~4 Å (65, 66). In the present study, the occurrence of cationic shells at 3.0–3.3 Å is not compatible with the exclusive formation of outer-sphere Co complexes.

The formation of inner-sphere surface complexes involves the creation of chemical bonds between the sorbate and the surface oxygens of the sorbent. Surface cations of the sorbent thus enter the second coordination sphere of the sorbate. If this next-nearest coordination sphere contains only cations from the sorbent, then adsorbed species are isolated on the sorbent surface and form mononuclear surface complexes (67). Here, only Mg and Si shells were detected at 3.03 and 3.27 Å, suggesting that Co form mononuclear inner-sphere surface complexes.

Polymerization of the sorbate in the vicinity of an inner-sphere surface complex may lead to the precipitation of a pure hydroxide phase, or a mixed one if dissolved species from the sorbent phase are incorporated in the precipitate (21). In the present study, this surface precipitate would be either $Co(OH)_{2(s)}$ or a neoformed (Co, Mg) hydrous silicate. Results from the quantitative spectral analysis, and the dissimilarity of EXAFS spectra for Co-sorbed hectorite, $Co(OH)_{2(s)}$ and CoKer (Fig. 9) suggest that no CoKer or $Co(OH)_{2(s)}$ did precipitate. The neoformation of a CoMgKer-like phase seems more possible, as EXAFS spectra for the sorption sample and CoMgKer are similar. However, these two compounds clearly have different $\chi_{2nd\ peak}(k)$ functions (Fig. 15), which indicates that Co do not have the same structural environments. Furthermore, if Co sorption resulted in the neoformation of a CoMgKer-like phase, then the amount of dissolved Mg would be expected to decrease, or its release rate by hectorite would be at least significantly slowed down shortly after Co introduction in the suspension. Instead, chemical experiments (68) showed that the release rate of Mg dramatically increases. Compelling neoformation of a (Co, Mg) hydrous silicate can thus be rejected.

Following its adsorption, the sorbed cation may also diffuse to vacant sites of the sorbent. For example, in dioctahedral smectites, where one third of octahedral sites are vacant, Ni(II) was shown to diffuse within empty sites upon heating at 150°C (8). The proportion of vacant sites is not known in hectorite, but it can be taken to 1% as in trioctahedral magnesian stevensites (69) which are isostructural to hectorite. For 1% of vacant sites, the amount of vacancies equals ~80 μmol g^{-1}, which is clearly higher than the amount of sorbed Co (37 μmol g^{-1}). Co

diffused into vacant octahedra would be surrounded by 6 (Mg, Li) octahedral neighbors (N_{oct}) and 4 Si tetrahedral neighbors (N_{tet}), leading to a N_{oct}/N_{tet} ratio of 1.5. In the sorption sample, $N_{tet} = N_{Si} = 2.2 \pm 0.5$, but N_{oct} is probably higher than N_{Mg}, because structural Li atoms are too light to contribute to the EXAFS signal. Assuming a random distribution of Li in the octahedral sheet, N_{oct} can be calculated from the stoichiometric composition of hectorite and is equal to $N^*_{Mg}(3/2.65) = 1.8 \pm 0.45$ for the sorption sample. N_{oct}/N_{tet} is thus equal to 0.8 ± 0.3, which is significantly different from the 1.5 expected if Co were in octahedral vacancies. This N_{oct}/N_{tet} value is also not consistent with a mixing of Co outer-sphere complexes and Co in vacancy sites. This discussion on the different possible sorption mechanisms of Co allows us to conclude that Co form inner-sphere mononuclear complexes at the surface of hectorite.

Location of Inner-Sphere Surface Complexes

Angular P-EXAFS measurements indicated that Co–Mg pairs are parallel to the plane of the hectorite film, whereas Co–Si pairs are inclined by ~70° from this plane. Since texture analysis showed that (Mg, Li) octahedral sheets are parallel to the film plane, then the only possible location for Co surface complexes is at the edges of hectorite platelets, in the prolongation of the octahedral sheet.

This conclusion is further supported by structural parameters derived from the quantitative analysis of EXAFS spectra. The $R_{Co–Mg}$ and $R_{Co–Si}$ distances of 3.03 and 3.27 Å are very close to the structural distances $d_{(Mg,Li)–(Mg,Li)} = 3.03$ Å and $d_{(Mg,Li)–Si} = 3.23$ Å for hectorite (54, 55). In addition, $\beta^{exp}_{Mg} \sim 80°$ and $\beta^{exp}_{Si} \sim 22°$ compare well with crystallographic β values for Mg–Mg ($\beta_{Mg} = 90°$) and Mg–Si ($\beta_{Si} \sim 30°$) pairs in hectorite. These similarities in distance and angle between surface Co and structural Mg indicate that these two atoms have similar (but not identical) structural environments. Based on these results, it is concluded that Co octahedra are located on the edges of hectorite platelets and share one or several edges with structural (Mg, Li) octahedra (E-type linkage) and one or several corners with Si tetrahedra (C-type linkage), like in a clay structure.

Structure of Co Surface Complexes on Hectorite

Surface Structure of Platelet Edges

Electron microphotography indicated that hectorite crystallites have a lath-type morphology and are elongated along the **a** direction (54, 70). The large (001) basal planes are bounded predominantly by (010) planes (90%), and, to a lesser extent, by (110), (120), and (100) planes. How the atomic structure of these boundary planes can be modeled from the crystal structure of hectorite will be developed for the (010) layer edge.

Idealized pristine surfaces can be obtained by truncating the hectorite bulk structure along planes perpendicular to the (001) surface and then by completing the broken coordination polyhedra with oxygens. For energetic reasons, truncation planes having the minimum number of broken Me–O–Me bonds (Me = Si or Mg) are likely favored. Two different surface configurations are obtained (Fig. 17): B1, in which surface oxygens of the octahedral sheet are uniquely coordinated to Mg, and B2, which is depleted in surficial Mg in comparison to B1, so that half of surface oxygens coordinated to Mg are also coordinated to Si.

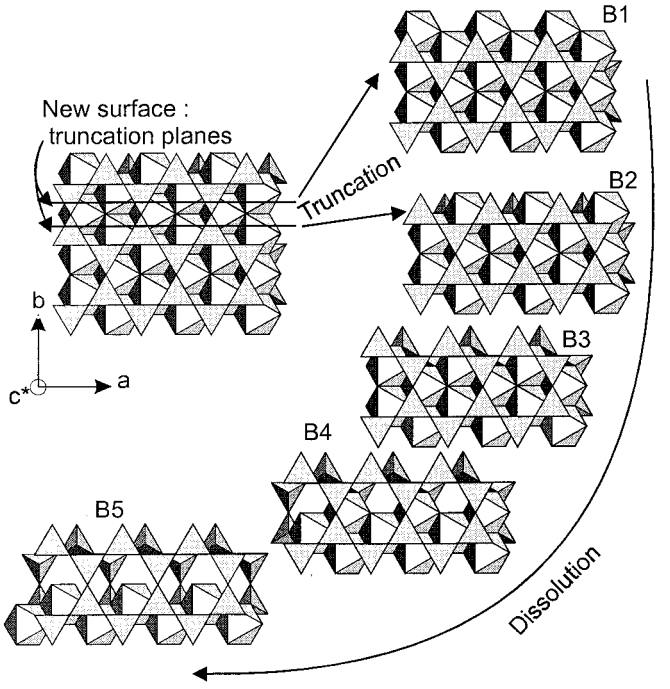

FIG. 17. Modeled formation of possible (010) layer edges from the bulk structure of hectorite. B1–B2 morphologies are obtained by truncation of the bulk structure, and B2–B5 are obtained by a progressive leaching of Mg.

These pristine surfaces can be altered by noncongruent dissolution, as dissolution takes place at layer edges. For example, chemical and microscopic studies on the dissolution of biotite in acidic conditions pointed to a rapid depletion of octahedral cations, leading eventually to the formation of amorphous silica fringes at layer edges (71). Preferential leaching of Mg was also observed for hectorite under slightly acidic conditions, but no silica fringes were identified (72). This preferential leaching can be modeled by deleting successive Mg rows at layer edges while leaving the tetrahedral sheets unaffected (Fig. 17). Obviously, most protruding Mg will be more easily removed, so that the B1 configuration is not expected to exist at pH ~6.5. But the absence of detected silica fringes on hectorite precludes an extensive depletion of surface Mg atoms. Finally, it can be assumed that layer edges have ideally a B2 surface structure in some places, and a more Mg-depleted structure elsewhere (B3 to B5). Figure 18 represents such an idealized surface structure for the (010) edge, which will be

used in the following for modeling the structure of Co surface complexes.

Structure of Surface Complexes on a (010) Edge

Several types of surface complexes may exist for each surface configuration. These complexes differ from each other by the number of E and C linkages, i.e., by the number of next-nearest cations from the octahedral and the tetrahedral sheets. For example, in the B2 configuration, adsorbed Co can form 3E and 2C linkages, or 1E and no C linkages (Fig. 19). These surface complexes will be denoted $S^{(010),B2}_{3E+2C}$ and $S^{(010),B2}_{1E+0C}$, respectively, where (010) is the plane index, B2 is the configuration index, and the subscript refers to the number of E and C linkages. For these two surface complexes, the number of E linkages exceeds that of C linkages by one, and therefore these complexes cannot account alone for experimental $N_{oct} = 1.8 \pm 0.45$ and $N_{tet} = 2.2 \pm 0.5$ values.

In the B3 surface configuration, sorbed Co can be bridged to either 3 (Mg, Li) and 4 Si ($S^{(010),B3}_{3E+4C}$), or to 1 (Mg, Li) and 2 Si ($S^{(010),B3}_{1E+2C}$) (Fig. 18). Assuming the formation of these two surface complexes only, with relative fractions x and y, respectively, the following set of equations is obtained:

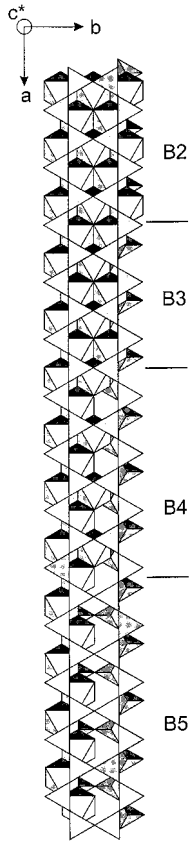

FIG. 18. Idealized (010) surface structure for hectorite projected along the **c*** direction.

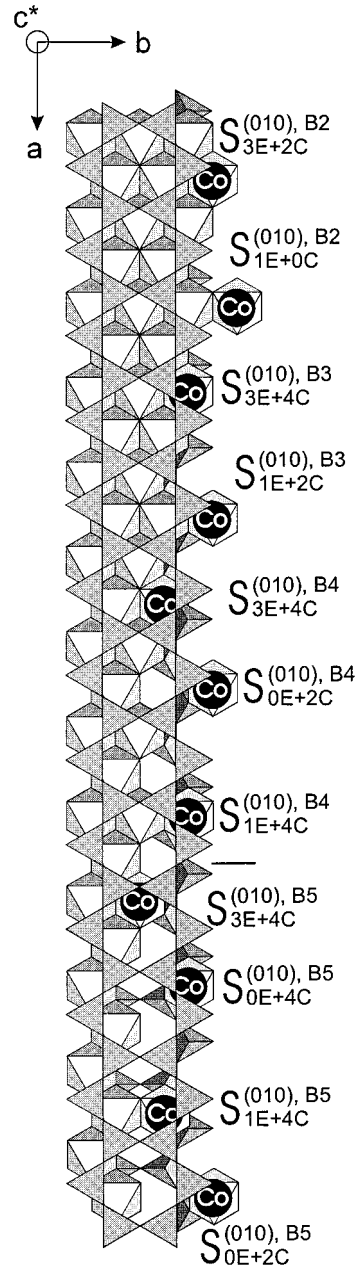

FIG. 19. Possible structure of mononuclear Co surface complexes on the (010) surface of hectorite. Co atoms are located in the plane of the (Mg, Li) octahedral sheet.

$$x + y = 1 \quad [17]$$

$$3x + y = N_{oct} \pm 0.45 \quad [18]$$

$$4x + 2y = N_{tet} \pm 0.5. \quad [19]$$

Expressing y as a function of x in Eq. [17] and substituting y for x in Eqs. [18] and [19] yields $x = 0.4 \pm 0.2$ (Eq. [18]) and $x = 0.1 \pm 0.25$ (Eq. [19]). Thus, x is comprised between 0.2 and 0.35, which means that, in this surface configuration,

$S^{(010),B3}_{3E+4C}$ and $S^{(010),B3}_{1E+2C}$ surface complexes would represent 20–35% and 65–80% of sorbed Co, respectively.

Three and four surface complexes may exist in B4 and B5 configurations, respectively: $S^{(010),B4}_{3E+4C}$, $S^{(010),B4}_{0E+2C}$, $S^{(010),B4}_{1E+4C}$, $S^{(010),B5}_{3E+4C}$, $S^{(010),B5}_{0E+4C}$, $S^{(010),B5}_{1E+4C}$, and $S^{(010),B5}_{0E+2C}$. None of these surface complexes can account alone for N_{oct} and N_{tet} values. Indeed, several types of surface complexes, possibly from different surface configurations (e.g., $S^{(010),B2}_{3E+2C}$, $S^{(010),B4}_{0E+2C}$, and $S^{(010),B5}_{1E+4C}$) are needed simultaneously to reproduce EXAFS results.

That EXAFS analysis yielded higher σ and lower N_O values for the sorption sample than for the references can now be explained by the coexistence of several types of surface complexes. Each type of surface complex differs from the others by N_{oct}, N_{tet}, and by the number of sorbent oxygens of the surface coordinated to Co. Therefore, Co–O bond strengths are expected to be scattered, which would eventually result in a slight dispersion of interatomic distances by some thousandths of Å. This dispersion provides a plausible explanation to the observed structural disorder.

Comparison with Previous EXAFS Studies

EXAFS results for Co sorbed on hectorite at moderate pH (pH 6.5) and surface coverage ($\Gamma = 0.32$ μmol g^{-1}) suggest that the percentage of Co–Co pairs is at most 10%, or that less than 2% of Co can be embedded in large polynuclear Co complexes. Mononuclear Co complexes were also observed on rutile for moderate chemical conditions (pH 5.9, $\Gamma = 0.62$ μmol g^{-1}). At higher pH (pH >6.7) and surface coverage ($\Gamma >$ 0.63 μmol g^{-1}) the formation of polynuclear Co complexes was reported for quartz (20, 73), kaolinite (66), alumina (65), and montmorillonite (9). In some studies these polynuclear complexes corresponded to mixed precipitates, having incorporated chemical species from the sorbent phase. For example, Towle *et al.* (65) suggested that Co sorption in an alumina suspension resulted in the formation of a Co–Al mixed hydroxide. Similarly, sorption of Co on quartz was shown to result in the neoformation of a Co-rich hydrous phyllosilicate (21). That no such precipitation did occur in the present study can be ascribed to the careful choice and control of chemical conditions throughout the whole sorption experiment.

CONCLUDING REMARKS

This study has demonstrated the potential of P-EXAFS for elucidating the geometrical arrangement of cations sorbed on clay minerals. Carefully controlled chemical conditions, and the elaboration of well-textured self-supporting films, are prerequisites to the successful application of this new method. In the present study, high ionic strength ($I = 0.3$ M) was chosen to favor pH-dependent sorption over cation-exchange adsorption, and a moderate pH of 6.5 allowed hindering the formation of polynuclear Co complexes as reported in previous studies.

P-EXAFS results indicate that, in the conditions of our experiments, Co form inner-sphere mononuclear surface complexes and are surrounded by two next-nearest cationic shells which are oriented differently with respect to the clay basal plane. The first subshell is parallel to the (001) plane and consists of ~1.6 ± 0.4 Mg atoms at 3.03 Å ($\beta_{Mg} = 80 \pm 10°$). The second is inclined by ~22.2° ± 1.4° to the **c*** direction and consists of 2.2 ± 0.5 Si atoms at 3.27 Å. No Co neighboring cations were detected, allowing us to disregard the presence of significant amounts of pure $Co(OH)_{2(s)}$ or Co-rich neoformed phyllosilicate. This whole set of structural results is consistent with the formation of Co mononuclear surface complexes located at the edges of hectorite platelets, in the continuity of the (Mg, Li) octahedral sheets.

ACKNOWLEDGMENTS

W. P. Gates is warmly thanked for fruitful discussions on clay mineral properties and sample preparations. The SRS, LURE, and ESRF staffs are acknowledged for providing the X-ray beam and for their technical assistance. D.C. acknowledges Professor M. Pernet for the opportunity of using the texture experiment at Laboratoire de Cristallographie-CNRS, Grenoble, France.

REFERENCES

1. McBride, M. B., "Environmental Chemistry of Soils." Oxford Univ. Press, Oxford, 1994.
2. Bruno, G., Decarreau, A., Proust, D., and Lajudie, A., *Appl. Clay Sci.* **7,** 169 (1992).
3. Konta, J., *in* "Euroclay Meeting" (J. Konta, Eds.), p. 11. Univerzita Karlova Praha, Prague, 1985.
4. Bailey, S. W., *in* "Crystal structures of clay minerals and their X-ray identification" (G. W. Brindley and G. Brown, Eds.). Mineralogical Society, London, 1980.
5. McBride, M. B., Pinnavaia, T. J., and Mortland, M. M., *Amer. Mineral.* **60,** 66 (1975).
6. McBride, M. B., *Clays Clay Min.* **27,** 91 (1979).
7. McBride, M. B., *Clays Clay Min.* **30,** 200 (1982).
8. Muller, F., Besson, G., Manceau, A., and Drits, V. A., *Phys. Chem. Minerals* **24,** 159 (1997).
9. Papelis, C., and Hayes, K. F., *Coll. and Surf. A: Physicochem. Engineer. Aspects* **107,** 89 (1996).
10. Chisholm-Brause, C. J., Conradson, S. D., Buscher, C. T., Eller, P. G., and Morris, D. E., *Geochim. Cosmochim. Acta* **58,** 3625 (1994).
11. Peigneur, P., Maes, A., and Cremers, A., *Clays Clay Min.* **23,** 71 (1975).
12. Inskeep, W. P., and Baham, J., *Soil Sci. Soc. Am. J.* **47,** 660 (1983).
13. Charlet, L., Schindler, P. W., Spadini, L., Furrer, G., and Zysset, M., *Aquatic Sci.* **55,** 291 (1993).
14. McKinley, J. P., Zachara, J. M., Smith, S. C., and Turner, G. D., *Clays Clay Min.* **43,** 586 (1995).
15. Zachara, J. M., Smith, S. C., Resh, C. T., and Cowan, C. E., *Soil Sci. Soc. Am. J.* **57,** 1491 (1993).
16. Zachara, J. M., and McKinley, J. P., *Aquatic Sci.* **55,** 250 (1993).
17. Zachara, J. M., and Smith, S. C., *Soil Sci. Soc. Am. J.* **58,** 762 (1994).
18. Scheidegger, A. M., Lamble, G. M., and Sparks, D. L., *Environ. Sci. Technol.* **30,** 548 (1996).
19. Scheidegger, A. M., Lamble, G. M., and Sparks, D. L., *J. Colloid Interface Sci.* **186,** 118 (1997).
20. O'Day, P. A., Brown, G. E. r., and Parks, G. A., *Geol. Soc. Amer. Abstr. Prog.* (1990).
21. Manceau, A., Schlegel, M. L., Nagy, K. L., and Charlet, L., submitted.

22. Teo, B. K., "EXAFS: Basic Principles and Data Analysis." Springer-Verlag, Berlin, 1986.
23. Manceau, A., Bonnin, D., Kaiser, P., and Fretigny, P., *Phys. Chem. Minerals* **16,** 180 (1988).
24. Manceau, A., Bonnin, D., Stone, W. E. E., and Sanz, J., *Phys. Chem. Minerals* **17,** 363 (1990).
25. Manceau, A., Schlegel, M. L., Chateigner, D., Lanson, B., Bartoli, C., and Gates, W. P., *in* "Synchrotron X-ray Methods in Clay Science" (D. Schulze, P. Bertsch, and J. Stucki, Eds.). Clay Mineral Society of America, in press.
26. Manceau, A., Chateigner, D., and Gates, W. P., *Phys. Chem. Minerals* **25,** 347 (1998).
27. Bunge, H. J., "Textures in Material Science." Butterworth, London, 1981.
28. Wenk, H. R., Chateigner, D., Pernet, M., Bingert, J., Hellstrom, E., and Ouladdiaf, B., *Physica C* **272,** 1 (1996).
29. Bonnin, D., Bouat, J., Kaiser, P., Frétigny, C., and Béguin, F., *J. Phys. C* **8,** 865 (1986).
30. Manceau, A., *Can. Miner.* **28,** 321 (1990).
31. Komadel, P., Madejova, J., Janek, M., Gates, W. P., Kirkpatrick, R. J., and Stucki, J. W., *Clays Clay Min.* **44,** 228 (1996).
32. Kreit, J. F., Shainberg, I., and Herbillon, A. J., *Clays Clay Min.* **30,** 223 (1982).
33. Jackson, M. L., "Soil Chemical Analysis." Prentice–Hall, Englewood Cliffs, NJ, 1964.
34. Zachara, J. M., Smith, S. C., and Kuzel, L. S., *Geochim. Cosmochim. Acta* **59,** 4825 (1995).
35. Anderson, S. J., and Sposito, G., *Soil Sci. Soc. Am. J.* **55,** 1569 (1991).
36. Tiller, K., *Clay Min.* **7,** 245 (1968).
37. Verburg, K., and Baveye, P., *Clays Clay Min.* **43,** 637 (1995).
38. Jeffery, G. H., Bassett, J., Mendham, J., and Denney, R. C., "Vogel's Textbook of Quantitative Chemical Analysis." Wiley, New York, 1978.
39. Iler, R. K., "The Chemistry of Silica," Wiley, New York, 1979.
40. Rimstidt, J. D., *Geochim. Cosmochim. Acta* **61,** 2553 (1997).
41. Stumm, W., and Morgan, J. J., "Aquatic Chemistry." Wiley, New York, 1996.
42. Cases, J-M., Berend, I., Delon, J. F., François, M., Grillet, I., Michot, L., Poirier, J. E., and Yvon, J., *in* "Matériaux argileux" (A. Decarreau, Eds.). Société française de minéralogie et de cristallographie, Paris, 1990.
43. Tröger, L., Zschech, E., Arvanitis, D., and Baberschke, *Jpn. J. Appl. Phys.* **32,** 144 (1992).
44. Castañer, R., and Prieto, C., *J. Phys. III France* **7,** 337 (1997).
45. Decarreau, A., *C.R. Acad. Sci. Paris* **292,** 61 (1981).
46. Decarreau, A., *Geochim. Cosmochim. Acta* **49,** 1537 (1985).
47. Matthies, S. M., Vinel, G. W., and Helming, K., "Standard Distributions in Texture Analysis." Akad. Verlag, Berlin, 1987.
48. Van der Hoek, M. J., Werner, W., and Van Zuylen, P., *Nucl. Instr. Meth. in Phys. Res. A* **246,** 380 (1986).
49. Aberdam, D., *J. Synchrotron Rad.* **5,** 1287 (1998).
50. Lengeler, B., and Eisenberger, P., *Phys. Rev. B* **21,** 4507 (1980).
51. Manceau, A., and Combes, J-M., *Phys. Chem. Minerals* **15,** 283 (1988).
52. Rehr, J. J., Albers, R. C., and Zabinsky, S. I., *Phys. Rev. Lett.* **69,** 3397 (1992).
53. Rayner, J. H., and Brown, G., *Clays Clay Min.* **21,** 103 (1973).
54. Oberlin, A., and Mering, J., *Bull. Soc. Franç. Minér. Crist.* **89,** 29 (1966).
55. Kadi-Hanifi, M., and Mering, J., *C.R. Séanc. Acad. Sc. Paris D* **274,** 149 (1972).
56. Lotmar, W., and Feitknecht, W., *Z. Kristallograph. Kristallogeom. Krystallphys. Krystallchem.* **93,** 368 (1936).
57. O'Day, P. A., Rehr, J. J., Zabinsky, S. I., and Brown Jr., G. E., *J. Am. Chem. Soc.* **116,** 2938 (1994).
58. Vaarkamp, M., Dring, I., Oldman, R. J., Stern, E. A., and Koningsberger, D. C., *Phys. Rev. B* **50,** 7872 (1994).
59. Scheidegger, A. M., Strawn, D. G., Lamble, G. M., and Sparks, D. L., *Geochim. Cosmochim. Acta* **62,** 2233 (1998).
60. Bowker, A. H., and Liebermann, G. J., "Engineering Statistics." Prentice–Hall, Englewood Cliffs, NJ, 1959.
61. Tröger, L., Arvanitis, D., Baberschke, K., Michaelis, H., Grimm, U., and Zschech, E., *Phys. Rev. B* **46,** 2383 (1992).
62. Shannon, R. D., *Acta Cryst. A* **32,** 751 (1976).
63. Hazen, R. M., and Wones, D. R., *Amer. Mineral.* **57,** 103 (1972).
64. Charlet, L., and Manceau, A., *in* "Environmental particles" (J. Buffle and H. P. Van Leeuwen, Eds.), Vol. 2, p. 117. Lewis, London, 1993.
65. Towle, S. N., Bargar, J. R., Brown Jr., G. E., and Parks, G. A., *J. Colloid Interface Sci.* **187,** 62 (1997).
66. O'Day, P. A., Parks, G. A., and Brown Jr., G. E., *Clays Clay Min.* **42,** 337 (1994).
67. Spadini, L., Manceau, A., Schindler, P. W., and Charlet, L., *J. Colloid Interface Sci.* **168,** 73 (1994).
68. Schlegel, M. L., Charlet, L., and Manceau, A., *J. Colloid Interface Sci.*, submitted.
69. Güven, N., *in* "Hydrous Phyllosilicates" (S. W. Bailey, Eds.), Reviews in Mineralogy, Vol. 19. Mineralogical Society of America, Washington, DC, 1988.
70. Mathieu-Sicaud, A., and Mering, J. *Bull. Soc. Franç. Minér. Crist.* **74,** 439 (1951).
71. Turpault, M.-P., and Trotignon, L., *Geochim. Cosmochim. Acta* **58,** 2761 (1994).
72. Tiller, K., *Clay Min.* **7,** 261 (1968).
73. O'Day, P. A., Chisholm-Brause, C. J., Towle, S. N., Parks, G. A., and Brown, G. E. J., *Geochim. Cosmochim. Acta* **60,** 2515 (1996).
74. Baes, C. F. J., and Mesmer, R. E., "The Hydrolysis of Cations." Wiley, New York, 1976.